Finite Elements in Analysis and Design 249 (2025) 104390

Contents lists available at ScienceDirect

Finite Elements in Analysis & Design

journal homepage: www.elsevier.com/locate/finel

Role of the interphase zone in the effective mechanical properties and fracture modes of multiphase metal matrix composites at microscale

Szymon Nosewicz *, Grzegorz Jurczak

Institute of Fundamental Technological Research, Polish Academy of Sciences, 5B Pawinskiego, 02-106, Warsaw, Poland

A R T I C L E I N F O

Keywords:
Metal matrix composite
Interphase
Finite element modelling
Fracture
Gurson–Tvergaard–Needleman model

A B S T R A C T

This study conducts a comprehensive numerical analysis to examine how the interphase zone influences the mechanical behavior of multiphase metal matrix composites at the microscale. A unit-cell model is developed within a finite element framework to capture the mechanical response of (a) interphase and particle deformation and damage, (b) a porous metal matrix, and (c) surface separation at two distinct interfaces. The material properties of the composite's key constituents are determined through a calibration process combining experimental testing and literature data. A series of simulations on unit-cell models with varying interphase characteristics are carried out to assess the effect of different plastic properties. Additionally, the role of interphase brittleness is investigated by modifying the failure strain to represent brittle, semi-ductile, and ductile behavior. By systematically varying interphase parameters, the study explores a broad spectrum of potential composite performance scenarios. Parametric studies are also conducted to analyze the behavior of interfaces between composite constituents. By adjusting cohesive strength and fracture energy, the model captures a wide range of bonding conditions—from weak to strong, and from brittle to ductile. The analysis identifies more than six distinct failure modes. Comparative stress-strain responses are used to highlight the influence of specific parameters on composite behavior. Key performance metrics such as toughness, ultimate tensile strength, and ductility are evaluated to illustrate the connection between microscopic features and macroscopic properties.

1. Introduction

Industry has an increasing need for new materials with high strength, ductility, wear resistance, thermal conductivity, and corrosion resistance. Composite materials based on metal matrixes, called Metal-Matrix Composites (MMCs), can solve such a demand due to their high strength-to-weight ratio, improved high-temperature strength retention, and creep and fatigue resistance. Various ceramic materials (e.g. SiC, Al_2O_3, TiC, and ZrO_2) can be applied to reinforce the metal matrix in different forms (particles, fibres, whiskers, etc.), combining the advantages of their properties [1–4]. However, MMCs are usually more complicated than just a two-phase material combination. Due to solubility and temperature-driven diffusion, another phase may form between the two phases of the composite, which exhibits properties quite different from those of its surroundings [5]. Such an interphase plays a critical role

* Corresponding author.
E-mail address: szymon.nosewicz@ippt.pan.pl (S. Nosewicz).

https://doi.org/10.1016/j.finel.2025.104390
Received 10 April 2025; Received in revised form 15 May 2025; Accepted 23 May 2025
0168-874X/© 2025 The Authors. Published by Elsevier B.V. This is an open access article under the CC BY license (http://creativecommons.org/licenses/by/4.0/).

[6] and modifies a composite's properties by changing its global mechanical behaviour [7–9].

There are generally two modelling approaches which predict interphase properties in inhomogeneous composite materials. The first approach assumes that the interphase region is a *zero-thickness interface* with appropriate mechanical conditions between the contacting surfaces. Hence, the three-phase composite configuration is replaced by an equivalent two-phase composite, where the interphase is reduced to a specific surface with appropriate interface properties. The parameters characterising the interface are mainly its strength, supported by slip conditions. Such an approach is well-suited to relatively thin interphases, with thicknesses not exceeding a few nanometers; no changes in physical or structural properties are observed across the interphases [10,11]. The specific behaviour of the composite interface can be described by various forms of constitutive relations, linking surface displacements and traction forces [12,13].

The Cohesive Zone Model (CZM) can be used to model such an interface [14–16]. Usually, a numerical approach based on the Finite Element Method (FEM) is used to study the effect of the interface strength on the composite strength and its damage type under different loadings [17–19]. This nonlinear elastic model of the interface assumes that normal and tangential tractions are continuous through the interface but are related to respective displacements at the interface in a nonlinear manner. For example, Zhang [17] investigated composite strengthening with interphase and showed that the matrix/interphase interface plays a more significant role than the interphase/particle one. Ben [20] applied a novel nonlinear cohesive law for a coated spherical particle with functionally graded interphase and estimated such a composite's interface strength and debonding strain. Qing [18] studied the ductile failure of the composite and assumed a damage model based on a simulated triaxial stress indicator. Cheng [19] proposed an interphase debonding criterion based on a statistical approach.

Another approach for estimating the effective properties of such inhomogeneous materials is to assume that the interphase region is *an extra layer* between the particle and the matrix. Its thickness is usually uniform or, less often, variable. Variation of the interphase physical properties is related to specific conditions of the composite fabrication, i.e. high-temperature diffusion, the mixing of molten regions, the formation of secondary nanoparticles in the interface, etc. Thus, interphase with its boundaries within the metal-ceramic composite should be treated as another structural element with specific characteristics, i.e. geometrical, structural, and mechanical properties, averaged through the interphase layer or graded between the particle and the matrix.

A micromechanical approach to modelling the global effect of the homogeneous interphase surrounding spherical particles was presented by Sarvestani [21] and Jiang [22]. The physical properties of the material and the geometrical parameters of the interphase (e.g. Young's modulus and interphase thickness) were assumed, in order to estimate the evolution of the debonding damage and elastoplastic response of the composite. A homogenisation methodology can also be applied to describe the effective physical properties of the homogeneous inclusion efficiently surrounded by heterogeneous interphase [23–26]. Within this approach, we may solve the problem within the framework of the classical theory of elasticity, by assuming values for the averaged strain field of the matrix (the Mori-Tanaka method) [27], effective matrix [28], and periodic structure [29], or by formulating a three-phase hypothesis [30].

Another approach, which assumes a multi-layered interphase model, was presented by Joshi [31]. He undertook continuum modelling of a multi-walled carbon nanotube reinforced composite with interphase in between, using a three-phase representative volume element (RVE), solved using a finite element approach. Another multi-layered interphase model used for the micromechanical modelling of the nanocomposite structures, and estimation of the interface damage during various loading modes, was presented by Shabana [32]. Choi [33] presented the concept of the multi-inclusion continuum model for polymer nanocomposites, in terms of elastic, elastoplastic, and thermoelastic behaviour, and explored the effect of nanoparticle size. Such an approach, which is a well-known interphase model in the literature, regards composite structure as a matrix reinforced by multi-phase-inclusions and exploits a continuum mechanical model (or sometimes uses a multiscale approach) to estimate the effective behaviour of the composite [26,31,32].

While theoretical modelling of the interphase behaviour can be challenging, computational modelling of such inhomogeneous structures seems to be conceptually less complicated. To study the effect of the interphase on the macroscopic mechanical properties of the composite, an elastic, elastoplastic, or viscoelastic model of inclusion, interphase, and matrix may be assumed. A thick interphase surrounds inclusions, usually with a simple geometry, and both are embedded in the matrix. The effective mechanical properties of the composites can be identified, as well as the equivalent continuum model for internal stress and strain fields. Finite element or finite difference methods are most extensively used to solve such a problem numerically [34–36]. The strengthening or weakening behaviour of the spherical particle-reinforced composite was numerically investigated by Zhang [17] using a cell model and finite element approach, with respect to the interphase's stiffness, thickness, and debonding location. Choi [33] studied the interphase's effective mechanical properties and geometry in a heterogeneous material using molecular dynamics and finite element simulations. Damage mechanisms and their relations with the macroscopic tensile properties of SiC-reinforced aluminium for three different interphase strengths were presented by Su [37]. Using the generalised self-consistent method combined with the Gurson damage model, he showed that interphase strength is a governing factor for damage propagation in the composite. The type and nature of interfacial bonding at the matrix/particle interfaces, as well as the effect of the interphase, were experimentally measured and numerically simulated by the use of 3D FEM by Veillère [36]. Jincheng [38] used the FEM approach, coupled with the cell modelling method, to simulate energy dissipation in the composite with a ductile interphase. Elastic stiffness and geometric relationships of the interphase were assumed to be parameters affecting energy dissipation during the cyclic external loading of a composite.

As presented in the state of the art in the topic of finite element modelling of mechanical behaviour of metal matrix composites with additional interphase, practically all numerical analyses are based on a single approach predicting a certain damage mode: interface failure or particle/interphase/matrix cracking. Such an assumption limits the deformation and damage investigation, thus it cannot reveal the full view of the complex phenomenon. Against the background of the literature review, the presented paper combines two main approaches for reproducing both the interphase and interface behaviour, as demonstrated by modelling: a) the interphase as a separate region with specific mechanical properties, and b) the interface as a zero-thickness contact bonding between the main composite components (particle-interphase and interphase-matrix). In that way, we considered most of the major deformation and damage effects in order to predict the final failure of the multiphase metal matrix composite as accurately as possible. Our work was motivated by two practical/experimental examples of interphase, which occurred during the authors' investigation of the manufacturing and microstructural/mechanical characterisation of metal matrix composites (Section 2). The novelty of proposed work is related to the application of three constitutive material models: the Gurson–Tvergaard–Needleman model for porous matrix damage; the elastic-plastic model with damage, for particle/interphase cracking; and the cohesive zone model for interface failure (Section 3), in numerical prediction of deformation and damage of multiphase composite with additional interphase zone. For the first time, three different modelling approaches were employed to reproduce the main fracture modes of such a non-trivial system. The aim is to check the broadest possible range of interphases and interfaces, starting from relatively brittle to extremely ductile and plastic ones (Section 4). Such parametric analysis is supposed to be a guidepost and a clue for our next level in the multiscale framework of multiphase composites.

2. Formulation of the problem

One of the central challenges for materials engineering, when dealing with multiphase composite materials, is to understand the behaviour of materials at the metal-ceramic interface. This interface is often governed by a "*third material*" (the interphase), which develops at the boundary between the matrix and the reinforcement. The characteristics of this interphase - its structure and morphology - can profoundly influence the overall properties of the composite. In some instances, unfavourable interphase formation can lead to brittle phases near the metal-ceramic zone, severely degrading the material's mechanical performance [6].

The origins of an interphase zone can be split into two types. Firstly, the interphase can be defined as the region between the ductile metal and the brittle ceramic phase created as the product of the chemical reaction of two main composite components; secondly, it could be the particular layer preventing the reaction. We emphasise these two topics by revealing the importance of considering the interphase zone on effective macroscopic behaviour.

2.1. Interphase as a product of the chemical reaction during manufacturing

In general, the manufacturing of multiphase materials is commonly combined with thermal treatment. For sintering materials with mutual solubility, intermediate phases with varying component concentrations may form during specific stages of the densification process. In this scenario, the reduction in the system's free energy is not only driven by the decrease in pore surface area but also by mutual diffusion, which either promotes material composition homogenisation or leads to the development of stable intermediate phases [39].

Some of the best examples of such multiphase materials with interphase are *nickel-silicon carbide composites*. Recently, numerous studies have examined the Ni-SiC system's behaviour at elevated temperatures [5,6,40,41]. Manufacturing/sintering brings significant structural evolution due to silicon carbide's partial (or complete) dissolution, driven by the extensive reaction between nickel and silicon. This process results in the formation of a multicomponent interphase characterised by a nickel silicide matrix ($Ni_{31}Si_{12}$ and/or Ni_3Si), enriched with carbon nanoprecipitates (Fig. 1). Prolonged thermal treatment causes these nanoprecipitates to grow, agglomerating into larger carbon particles and becoming segregated at the interface between the nickel matrix and the interphase.

Alongside significant microstructural transformations, the fabricated composites exhibit diverse mechanical properties [6]. Compared to the pure nickel sample, the addition of silicon carbide particles, with the development of NiSi interphase between the metal and ceramic phase, affects the deformation behaviour, causing it to be more brittle and, as a consequence, reducing elongation to 0.10–0.75 %, from the 39 % of pure nickel. Moreover, composites characterised by the presence of a NiSi interphase indicate a drop of the ultimate tensile strength by around 50 %, which fully confirms the pessimistic scenario of interphase impact.

Another example of interphase development, due to chemical interaction between the metal and ceramic phase, is related to the Additive Manufacturing (AM) processes, e.g. Select Laser Melting (SLM). Several works have reported the formation of an interlayer with altered properties [42–44]. In the first example [42], SLM was used to fabricate a new type of Interpenetrating Phase and special attention was drawn to the influence of the interphase between titanium and WC-Co phases. Due to the large extent of the interphase

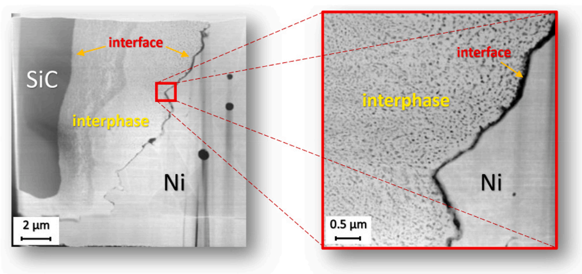

Fig. 1. SEM images of nickel-silicon carbide composites as an example of metal matrix composite with an additional third phase (interphase) created as the product of the chemical reaction [5].

area and the presence of a plastic Ti phase, a relatively low elastic modulus of the Interpenetrating Phase Composites (IPCs) was recorded.

2.2. Interphase as a layer preventing the reaction during manufacturing

To avoid changes in the contact point between the metal and the ceramics, it is usually necessary to use a protective layer to block the diffusion process and phase reactions [45]. There are several methods for coating the ceramics with a metallic layer, including electrodeposition, chemical vapour deposition, physical vapour deposition, and magnetron sputtering [46–49]. The chemical vapour deposition of nickel and tungsten on silicon carbide particles has recently been employed to minimise the dissolution of silicon to copper during the sintering of Cu-SiC composites (see Fig. 2) [45,50].

All of the examined coatings protected SiC against decomposition, as there was no evidence of silicon dissolution in the copper matrix. The application of metallic coatings significantly enhanced the strength of the composite, keeping the ductility at the same level as that of composites without protection. Additionally, measurements of interfacial bonding strength [51] have confirmed the beneficial effect of the nickel and tungsten coatings on enhancing the strength of the interface between the matrix and the reinforcing particles.

3. Finite element framework of multiphase metal matrix composite

3.1. Numerical set-up of multiphase material simulation

The numerical investigation was based on a unit-cell approach to model the deformation and damage of metal matrix composites with interphase. The main goal for the numerical modelling was to determine the effect of the following on the macroscopic behaviour of multiphase MCCs.

- *the interphase,* treated as the additional phase located between the metal matrix and ceramic reinforcement;
- *the interfaces*, treated as the contact bonding between: a) particle and interphase, b) matrix and interphase.

This approach assumed various interphase and interfacial properties, to analyze composite global behaviour.

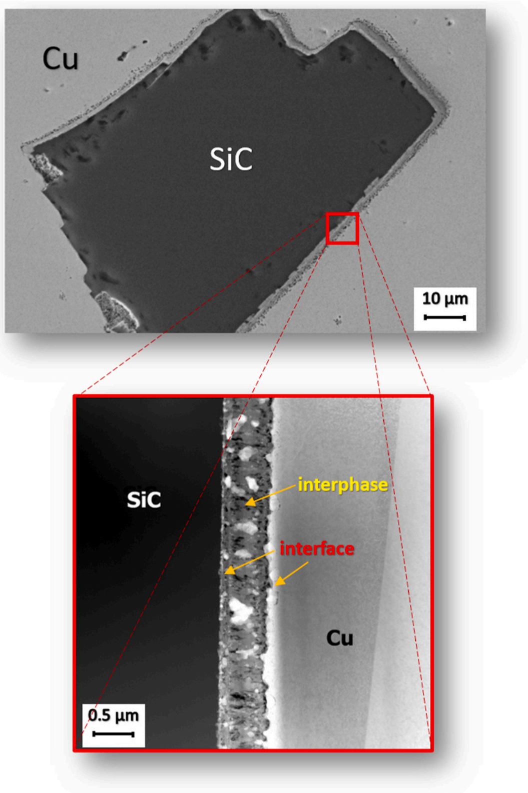

Fig. 2. SEM images of copper-silicon carbide composites as an example of a metal matrix composite with an additional third phase (interphase) as the particular layer preventing the unwanted chemical reaction [45].

3.1.1. Geometrical model of the multiphase composite sample

The numerical procedure comprised FE analysis within the ABAQUS software [52]. The scope of the geometrical model and simulation set-up, shown in Fig. 3, is based on SEM images of nickel-based composites (Fig. 1). We assumed a 17 x 17 × 27.5 μm unit-cell sample containing spheroidal ceramic particles surrounded by a homogeneous interphase layer with constant thickness. The elongated shape of the particle inclusion was consistent with the direction of elongation and experimentally observed shape of the ceramic particles (Fig. 1). The radius of the spherical ends of the particles was equal to 4.5 μm, while the central cylindrical part of the particles was 6.9 μm long. The total length of a particle was, therefore, 15.9 μm. The uniform thickness of the interphase was fixed at 2.4 μm. A metal matrix filled the rest of the domain in the cuboid sample. The dimensions of the sample can be scaled down to obtain a nanosized domain in order to reproduce the nanocomposite case. Moreover, it is expected that numerical model can be suitable for different forms of ceramic reinforcement in the form of (carbon) nanotubes or (graphene) nanoplatelets [53–55].

The presumed geometry of the composite FEM unit-cell model components yielded approximately 70/20/10 % of the volume fraction in the model, respectively, for matrix/interphase/particle parts. When manufacturing and characterising particle-reinforced composites, such an initial composition balancing an metal (80 %) and ceramic phase (20 %) content seems well-suited [5]. As we consider the creation of interphase as the result of phase transformation during the sintering process, we can assume that about half of the ceramics particle was transformed, together with a similar volume of the metal matrix, into the interphase creating a uniform layer around the particle covering an assumed 20 % volume fraction [6].

3.1.2. Boundary conditions of uniaxial tensile test simulation

The unit-cell sample presented above underwent a uniaxial tensile test; therefore, relatively simple Boundary Conditions (BCs) may be used. From a theoretical point of view, kinematic bounds at the ends of the sample seem to be sufficient for modelling uniaxial stretching. However, as our FE setup only covers a unit-cell domain with a single particle (a small part of the actual sample considered on a microscopic scale), we applied additional boundary conditions to simulate interaction with the adjacent bulk material. An extra boundary conditions, in the form of Multi-Point Constraints (MPCs), were assumed (Fig. 3) on four outer surfaces of the sample, perpendicular to the elongation direction. MPCs applied on the surface limit the free displacement of all nodes on the surface by calculating averaged displacement, common for all nodes. MPCs usually concern single component of the displacement vector - perpendicular to the surface. Averaged contraction or expansion of the sample, perpendicular to the surface under MPCs is calculated to minimise energy of the sample, and averaged displacement is applied to all nodes, maintaining the flatness of the surface (what is necessary to keep geometrical compatibility with identical adjacent sample).

MPCs applied on outer surfaces of the unit-cell sample copy mutual interaction between the matrix of adjacent unit-cells what modifies scheme of sample contraction or expansion. High symmetry of our sample assures adequacy of this approach and compliance with common Periodic Boundary Conditions where instead of surface linkage a set of node-to-node links is used to calculate displacement on the sample boundary.

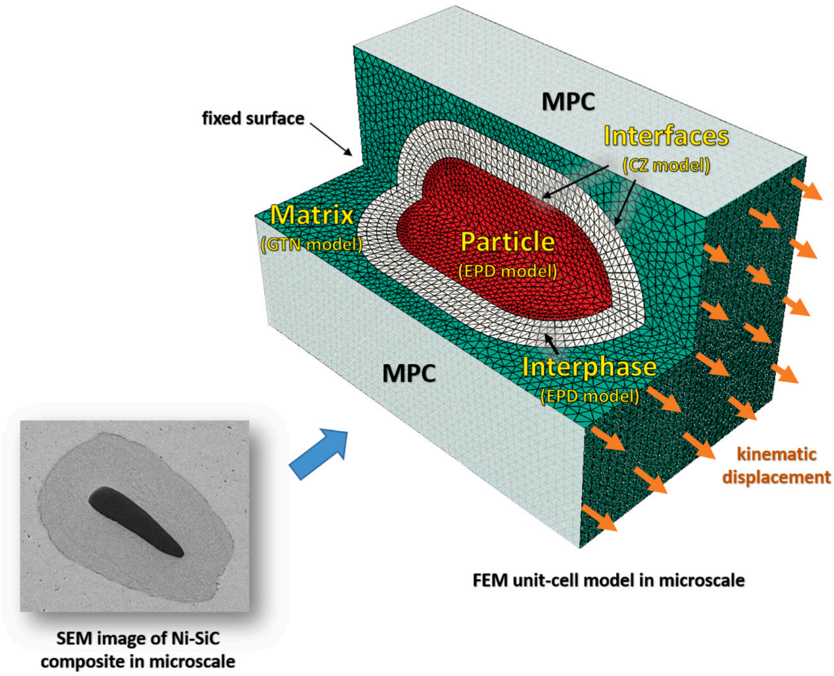

Fig. 3. Numerical set-up of a unit-cell model of metal matrix composite with additional interphase.

3.1.3. The meshing procedure of multiphase composite sample

As we consider the meshing procedure of the unit-cell sample consisting of three independent phases connected at two interfaces, the two aspects should be addressed clearly – mesh coherency and size-dependence. Finite element discretisation uses the general linear 3D tetrahedral solid elements (C3D4) from the ABAQUS elements library. Volume of each phase within the RVE volume was meshed independently, governed by sets of mesh seeds controlling the nodes/elements count and their size. Elements and nodes composing adjacent interfaces perfectly fit each other due to a proper adjustment of the above-mentioned mesh seeds. Keeping same number of nodes within the contact surface, we ensure mesh coherency, which seems to be essential for modelling stress transfer through the interphase as an extra layer between the particles and metal matrix.

Secondly, it is well known that FE simulations of material deformation and damage (especially using the Gurson–Tvergaard–Needleman model) are highly sensitive to mesh size. This dependency arises from material softening caused by damage growth, leading to high stress and strain gradients in the failure region. For a given applied displacement, the deformation calculated at Gauss points near the failure zone is greater for finer meshes, resulting in earlier failure initiation [56]. Two primary approaches are commonly used to address this issue. The first involves treating the mesh size as a material parameter that must be calibrated [57,58]. The second approach mitigates mesh size dependency by employing a non-local material model. A comprehensive review of these methods and the effects of mesh size on GTN model results can be found in Ref. [56]. The first approach was adopted in this study. Several different mesh sizes were utilised to investigate the influence of mesh resolution. Finally, the FE mesh used for the calculations was based on approximately 71k nodes, which resulted in 368k C3D4-type elements (Fig. 3).

3.1.4. Dynamic issues of FE simulations

The finite element calculations utilised dynamic analysis with explicit time integration. Such an approach must select appropriate time-displacement relations to avoid inertia effects during the simulations. Here, we assumed the amplitude definition based on the quadrant of the sine function. The initial, very small, time steps are the key to avoiding dynamic instabilities at the beginning of the process. At the same time, the subsequent increase in the displacement amplitude allowed us to complete the calculations in a reasonable amount of time. After several tests, we confirmed that the time process in the range 1.0–2.5 [s] was safe to calculate the dynamic process of the composite damage, corresponding to a deformation rate in the range 2–5 nm/s at the beginning of the process and 2.4–6.0 μm/s at the end.

3.1.5. Evaluation of macroscopic parameters

After the simulations, the effective stress-strain curves were prepared. Effective stress was calculated as the ratio of the sum of the axial reaction forces over the nodes on the surface subjected to kinematic loading, and the surface area. The effective strain was defined as the ratio of the displacement of the surface subjected to kinematic loading to the initial length of the sample. Based on these curves, we determined several effective parameters for evaluating the mechanical properties of multiphase composites.

- **Ultimate Tensile Strength (UTS)** is the maximum stress a material can withstand when stretched, before necking occurs; it represents the highest point on the stress-strain curve during a tensile test.
- **Ductility** is defined as a measure of the ability of a material to deform plastically before fracturing. It is typically expressed as a percentage elongation, which is defined as the ratio of the maximum sample displacement to the initial length.
- **Toughness** measures a material's ability to absorb energy and plastically deform before fracturing. It represents the material's capacity to withstand both elastic and plastic deformation under stress and its ability to resist breaking under impact or sudden loads. Toughness in a tensile test is defined as the area under the stress-strain curve.

3.1.6. Constitutive material models

The heterogeneous structure of a multiphase composite has been represented by several constitutive material models addressed to each composite component. Fig. 3 shows the distribution of the parts with an assigned specific model.

- **Gurson–Tvergaard–Needleman** (GTN) model: used to predict the deformation and damage evolution of the metal matrix, a key composite material component. GTN is rooted in micromechanics and is widely used in finite element analysis to simulate ductile failure in bulk and porous materials [59–63].
- **Elastic-plastic model with damage** (EPD): aimed at simulating the mechanical responses of particle and interphase components, where the interphase properties are the primary issues.
- **Cohesive Zone Model** (CZM): utilised to model the failure of two interfaces between composite components. The model effectively predicts the initiation and progression of cracks and delamination in materials [14–16,64–66].

Applying the above-mentioned material models should ensure the best representation of the multiphase metal matrix composites as complex materials and various mechanical effects during the simulations. The detailed formulation of each model is presented in sections 3.2-3.4.

3.2. Gurson–Tvergaard–Needleman model

Metal matrices typically exhibit highly heterogeneous local properties due to their granular structure. Grain boundaries and individual grains are randomly distributed, leading to varying combinations of strength and ductility, depending on their orientation.

Additionally, the matrix structure often contains residual porosity, an undesirable feature that remains after the manufacturing process.

Here, the heterogeneous structure of the metal matrix was modelled as a homogeneous medium using the GTN constitutive material law. The GTN model, originally developed to describe ductile failure through void nucleation and growth in homogeneous metallic materials [59], has also been applied to characterise the failure behaviour of MMCs [63]. In this study, we selected pure nickel as the representative material for finite element (FE) modelling. The nickel matrix is assumed to exhibit ductile behaviour, generating a significant number of micro-voids that grow rapidly and lead to the final failure. Residual porosity, resulting from the sintering process, is considered to be the primary source of local degradation. The formation and growth of individual micro-voids, culminating in crack initiation and propagation, ultimately cause the ductile nickel matrix to fail.

The yield function, initially proposed by Gurson [59], is defined as follows:

$$\Phi\left(\sigma_{\mathrm{e}}, \sigma_{\mathrm{h}}, \sigma_{\mathrm{y}}, f\right) = \left(\frac{\sigma_{\mathrm{e}}}{\sigma_{\mathrm{y}}}\right)^2 + 2q_1 f^* \left(\frac{3q_2\sigma_{\mathrm{h}}}{2\sigma_{\mathrm{y}}}\right) - \left(1 + q_3 f^{*2}\right) \tag{1}$$

where σ_{e} is the Mises equivalent stress, σ_{h} is the hydrostatic stress, σ_{y} is the yield stress, and f is the void volume fraction. Material parameters q_1, q_2, and q_3 were introduced by Tvergaard [67], as well as the modified void volume fraction f^* proposed by Tvergaard and Needleman [60], to model the decline of stress-carrying capacity during ductile fracture (void initiation, growth, and coalescence):

$$f^* = \begin{cases} f, \; f \le f_{\mathrm{c}} \\ f_{\mathrm{c}} + \dfrac{f_{\mathrm{u}}^* - f_{\mathrm{c}}}{f_{\mathrm{F}} - f_{\mathrm{c}}}(f - f_{\mathrm{c}}), \; f > f_{\mathrm{c}} \end{cases} \tag{2}$$

where the parameter f_{c} is the critical value of the void volume fraction, f_{F} is the value of the void volume fraction at which there is a complete loss of stress-carrying capacity in the material, and $f_{\mathrm{u}}^* = 1/q_1$ is the ultimate void volume fraction. The evolution equation for the void volume fraction is described as follows:

$$\dot{f} = \dot{f}_{\mathrm{growth}} + \dot{f}_{\mathrm{nucleation}} \tag{3}$$

where $\dot{f}_{\mathrm{growth}}$ is change due to the growth of existing voids and $\dot{f}_{\mathrm{nucleation}}$ is change due to the nucleation of new voids. $\dot{f}_{\mathrm{growth}}$ is based on the law of conservation of mass, in the form:

$$\dot{f}_{\mathrm{growth}} = (1 - f) \cdot \dot{\varepsilon}_{ii}^{\mathrm{pl}} \tag{4}$$

where $\dot{\varepsilon}^{\mathrm{pl}}$ is the plastic strain rate tensor and $\dot{f}_{\mathrm{nucleation}}$ is defined to obey a Gaussian distribution, given by:

$$\dot{f}_{\mathrm{nucleation}} = A\dot{\bar{\varepsilon}}^{\mathrm{pl}} \tag{5}$$

where $\dot{\bar{\varepsilon}}^{\mathrm{pl}}$ is the equivalent plastic strain rate, while

$$A = \frac{f_{\mathrm{n}}}{\mathrm{S_n}\sqrt{2\pi}} \exp\left(-\frac{1}{2}\left(\frac{\bar{\varepsilon}^{\mathrm{pl}} - \varepsilon_{\mathrm{n}}}{\mathrm{S_n}}\right)^2\right) \tag{6}$$

where f_{n} is the void volume fraction of nucleating particles, and $\mathrm{S_n}$ and ε_{n} are the standard deviations and the mean value of the distribution of the equivalent plastic strain.

The mechanical properties of the nickel matrix, provided as input model parameters, were evaluated using the calibration procedure. The input parameters related to elastic, plastic, and damage regime were tuned and fitted to the experimental results of the uniaxial tensile testing of the pure nickel sample, as shown in Section 4.2.

3.3. Elastic-plastic model with damage

3.3.1. Model formulation

An elastic-plastic model assuming isotropic, rate-independent plastic deformation is commonly used for metal plasticity calculations [68,69]. It assumes isotropic hardening and additive strain rate decomposition:

$$d\varepsilon = d\varepsilon^{\mathrm{el}} + d\varepsilon^{\mathrm{pl}} \tag{7}$$

Assumed isotropic hardening and linear elasticity can be described by using only two material parameters, i.e. Young's modulus E and Poisson's ratio ν or the related bulk K and shear modulus G. The total stress tensor can be decomposed into a volumetric component:

$$p = -\frac{1}{3}\mathrm{tr}(\boldsymbol{\sigma}) \tag{8}$$

and a deviatoric component:

$$\boldsymbol{S} = 2G\boldsymbol{\varepsilon}^{\mathrm{el}}. \tag{9}$$

The plastic flow rule is:

$$d\boldsymbol{\varepsilon}^{\mathrm{pl}} = d\overline{\varepsilon}^{\mathrm{pl}}\frac{3}{2}\frac{\boldsymbol{S}}{\sqrt{\frac{3}{2}\boldsymbol{S}:\boldsymbol{S}}} = d\overline{\varepsilon}^{\mathrm{pl}}\frac{3}{2}\frac{\boldsymbol{S}}{q} = d\overline{\varepsilon}^{\mathrm{pl}}\boldsymbol{n}, \tag{10}$$

where $d\overline{\varepsilon}^{\mathrm{pl}}$ is the scalar equivalent of the plastic strain rate, $\boldsymbol{n}$ is the flow direction, and q is the Mises equivalent stress. The relationship between uniaxial stress and plastic strain, in the case of temperature and strain-rate independent plasticity, leads to the yield condition:

$$q = \sigma^0\left(\overline{\varepsilon}^{\mathrm{pl}}\right) \tag{11}$$

where σ^0 is the yield stress defined by the user, as a function of equivalent plastic strain $\overline{\varepsilon}^{\mathrm{pl}}$. If the equivalent stress parameter q, calculated based on the purely elastic response, exceeds σ^0, it means that plastic flow occurs and the above equations must be integrated and solved for the state at the end of the consequent increments. Backward Euler integration is applied to the flow rule to give the plastic strain increment:

$$\Delta\boldsymbol{\varepsilon}^{\mathrm{pl}} = \Delta\overline{\varepsilon}^{\mathrm{pl}}\boldsymbol{n}. \tag{12}$$

The increment of the elastic component of the strain $\Delta\boldsymbol{\varepsilon}^{\mathrm{el}}$, calculated from the integrated plastic strain rate, combined with the deviatoric elasticity at moment t, gives:

$$\boldsymbol{S} = 2\mathrm{G}\left(\boldsymbol{\varepsilon}^{\mathrm{el}}\big|_t + \Delta\boldsymbol{\varepsilon} - \Delta\overline{\varepsilon}^{\mathrm{pl}}\boldsymbol{n}\right). \tag{13}$$

Finally, the Mises equivalent stress q must satisfy the uniaxial form defined above and, after some transformation, we obtain the following equation, which needs to be solved:

$$3\mathrm{G}\left(\sqrt{\frac{2}{3}\left(\boldsymbol{\varepsilon}^{\mathrm{el}}\big|_t + \Delta\boldsymbol{\varepsilon}\right):\left(\boldsymbol{\varepsilon}^{\mathrm{el}}\big|_t + \Delta\boldsymbol{\varepsilon}\right)} - \Delta\overline{\varepsilon}^{\mathrm{pl}}\right) - \sigma^0 = 0. \tag{14}$$

In our cases, the assumed type of plastic hardening is far from the ideal plasticity and, therefore, the equation is nonlinear. It is solved with respect to the equivalent plastic strain $\Delta\overline{\varepsilon}^{\mathrm{pl}}$ by using Newton's method, iterating until convergence is achieved. Once $\Delta\overline{\varepsilon}^{\mathrm{pl}}$ is known, the solution at a given step is fully defined:

$$\boldsymbol{S} = \frac{2\mathrm{G}}{1 + \frac{3\mathrm{G}}{q}\Delta\overline{\varepsilon}^{\mathrm{pl}}}\left(\boldsymbol{\varepsilon}^{\mathrm{el}}\big|_t + \Delta\boldsymbol{\varepsilon}\right). \tag{15}$$

To model plastic material damage, we assumed criteria related to nucleation, growth, and the coalescence of voids. The model assumes that the equivalent plastic strain $\Delta\overline{\varepsilon}_D^{pl}$ (that initiates the damage process) is a function of stress triaxiality:

$$\eta = \frac{-p}{q} \tag{16}$$

and plastic strain rate $\dot{\overline{\varepsilon}}^{\mathrm{pl}}$, as follows:

$$\overline{\varepsilon}_{\mathrm{D}}^{\mathrm{pl}} = \overline{\varepsilon}_{\mathrm{D}}^{\mathrm{pl}}\left(\eta, \dot{\overline{\varepsilon}}^{\mathrm{pl}}\right). \tag{17}$$

The damage is initiated when the state variable ω_{D} reaches 1:

$$\omega_{\mathrm{D}} = \int \frac{d\overline{\varepsilon}^{\mathrm{pl}}}{\overline{\varepsilon}_{\mathrm{D}}^{\mathrm{pl}}(\eta, \dot{\overline{\varepsilon}}^{\mathrm{pl}})} = 1. \tag{18}$$

At each time increment during the calculations, the increase of the state variable $\Delta\omega_{\mathrm{D}}$ is computed as:

$$\Delta\omega_{\mathrm{D}} = \frac{\Delta\overline{\varepsilon}^{\mathrm{pl}}}{\overline{\varepsilon}_{\mathrm{D}}^{\mathrm{pl}}(\boldsymbol{\eta}, \dot{\overline{\varepsilon}}^{\mathrm{pl}})} \geq 0. \tag{19}$$

Equivalent plastic stress $\overline{\sigma}_0^{\mathrm{pl}}$ and equivalent plastic strain $\overline{\varepsilon}_0^{\mathrm{pl}}$ at the moment of damage initiation ($\omega_{\mathrm{D}} = 1$) describes the state of the material at that moment; overall damage variable D is equal to 0. Equivalent plastic strain at failure $\overline{\varepsilon}_f^{\mathrm{pl}}$ defines the moment of the total failure of the material, at which overall damage variable D reaches a value of 1, as depicted in Fig. 4.

Within finite element analysis, the value of the equivalent plastic strain at failure $\overline{\varepsilon}_f^{\mathrm{pl}}$ (failure strain) depends on the characteristic length of the finite element. Hence, an identical mesh must operate with failure strain and ensure identical plastic behaviour.

Alternatively, equivalent plastic displacement at the point of failure $\overline{\delta}_f^{pl}$ or fracture energy dissipation G_f may be specified. The evolution equation describing the equivalent change in plastic displacement can be written as follows:

$$\dot{\overline{\delta}}^{pl} = L\dot{\overline{\varepsilon}}^{pl}, \tag{20}$$

where L is the characteristic length of the FE mesh. The evolution of the damage variable D between initiation and failure states (0–1) can be assumed in various forms, e.g. as a linear function, which leads to the following:

$$\dot{D} = \frac{L\dot{\overline{\varepsilon}}^{pl}}{\overline{\delta}_f^{pl}} = \frac{\dot{\overline{\delta}}^{pl}}{\overline{\delta}_f^{pl}} \quad . \tag{21}$$

When the effective plastic displacement $\overline{\delta}^{pl}$ reaches the value at the failure point, the material stiffness is fully degraded ($D = 1$) and the elements affected by failure should be deleted from the mesh.

3.3.2. *Material model parameters*

An elastic-plastic model with damage was applied, to anticipate the micromechanical performance of both the ceramic particles and interphase. For a ceramic component of the multiphase composite, silicon carbide (SiC) was chosen as the representative material, due to its mechanical specificity characterised by high strength and high brittleness [70,71]. We assumed the elastic properties of the SiC particle (Table 1) to be isotropic, represented by a Young's modulus equal to 450 GPa and a Poisson's ratio of 0.14, with an average tensile strength of 500 MPa [72]. To model the brittle behaviour of a SiC particle in a composite, we employed an elastic-plastic model with damage, where particle failure occurred almost immediately after reaching yield stress. A minor value of failure strain, set to 0.001, made the plastic behaviour of SiC particles almost meaningless. After initiation at one point, it caused the particle to fail and propagate immediately through the entire particle, making it very brittle, as intended. The plastic hardening curve, required by the elastic-plastic model to reproduce the plastic regime, is defined by the Swift formula [73,74]:

$$\sigma(\varepsilon_p) = K(\varepsilon_0 + \varepsilon_p)^n, \tag{22}$$

where K is the strength coefficient, n is the strain hardening exponent, and ε_0 is the initial strain.

Similar to ceramic particles, the interphase of the composite was modelled by an elastic-plastic model with damage. Unlike the well-known properties of the ceramic particle and metal matrix, determining the properties of the Ni-SiC interphase is challenging. On the one hand, it is analogous to the Ni-SiC composite with interphase (Fig. 1), which results from the temperature-driven diffusion between brittle SiC particles and the ductile Ni matrix. It may be assumed that its material properties are intermediate between these two phases and may vary over a wide range, depending on the parameters of the sintering process. On the other hand, we may not focus on the Ni-SiC composite but attempt to investigate the MMC behaviour, assuming that the theoretical interphase is a brittle, semi-ductile, or ductile material.

Here, we proposed four plastic types of interphase properties (denoted as I_1-I_4). They differed in their yield stress σ_y and the character of the hardening curve defined by the Swift parameters K and n (Table 1). The curves are plotted in Fig. 5, together with various values of interphase failure strain (ε_f^{pl} = 0.01, 0.1, and 0.3), marked as vertical lines, to illustrate the moment of material failure. So, in this way, we covered a wide range of possible interphase behaviours, from low to high strength and brittle to ductile material.

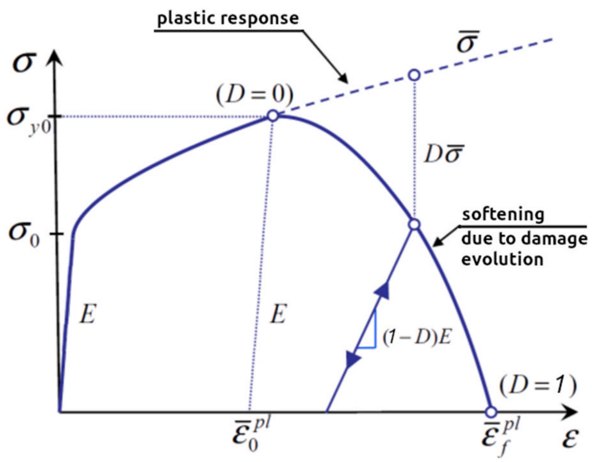

Fig. 4. Stress-strain curve showing progressive degradation with damage initiation and failure points.

Table 1

Elastic and plastic properties of FE simulations of tensile testing of a silicon carbide particle and different plastic types of interphase (I_1-I_4).

Parameter/ material	Theoretical density ρ_t [kg/m^3]	Young's modulus E [GPa]	Poisson's ratio ν	Yield stress σ_y [MPa]	Strength coefficient K [MPa]	Strain hardening exponent n	Initial strain ε_0
Silicon carbide	3120	450	0.14	500	980	0.20	0.02
Interphase I_1	5000	150	0.31	125	550	0.20	0.03
Interphase I_2					1360	0.46	0.03
Interphase I_3				375	550	0.20	0.03
Interphase I_4					1360	0.46	0.03

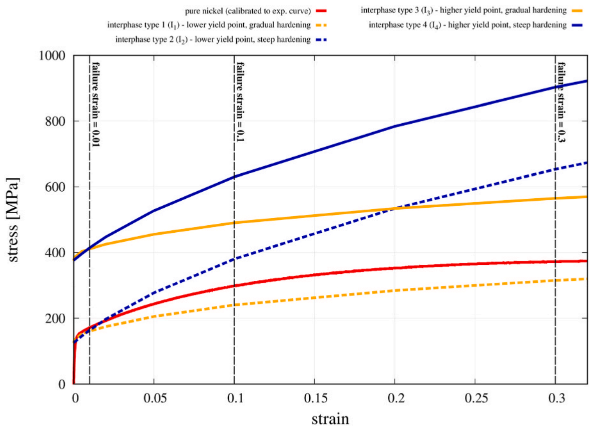

Fig. 5. Selected hardening curves (I_1-I_4) applied as the different plastic behaviour of various types of interphases (**brittle** - $\varepsilon_f^{pl} = 0.01$, **semi-ductile** - $\varepsilon_f^{pl} = 0.1$, and **ductile** - $\varepsilon_f^{pl} = 0.3$).

3.4. Cohesive zone model of the interface

In general, metal matrix composites indicate the weakest structural components in the metal-ceramic interface [75]. Modelling the mechanical behaviour of contact bonding between different phases is quite challenging, due to the complexity of various effects, such as different crystallographic systems and orientations at the interface, lattice mismatch, particle separation, or dislocation concentration [76]. To model the complex behaviour of the composite interfaces on a microscopic scale, we assumed particle/interphase and interphase/matrix transition surfaces to be cohesive zone (CZ) layers. This indicates a zero thickness layer with a specific traction–separation relation. Such an approach has been applied to successfully simulate a variety of material interfaces [14,15].

The key role of the CZ model is the traction-separation law, which allows us to consider the nature of the interface damage. In our case, we used the bilinear cohesive law presented in Fig. 6. The traction forces at the interface increase linearly, reach a maximum, and then decrease to zero, permitting a complete de-cohesion. During both the increasing and decreasing phases of the process, traction forces (and stresses) are proportional to the gap between the layers; the initial proportionality coefficient is called 'penalty stiffness' K_p. Here, we assumed that K_p equals 10^{14} N/m^3, within the suggested range of 10^{13}–10^{17} N/m^3 [77], what ensures compatibility with the model of an ideal interphase interface. If any component of the stress tensor (normal σ_n or shearing τ_s, τ_t) reaches the given value T_* (* denoted for n-normal, s-shear, and t-tangential), it means that damage is initiated within the cohesive layer:

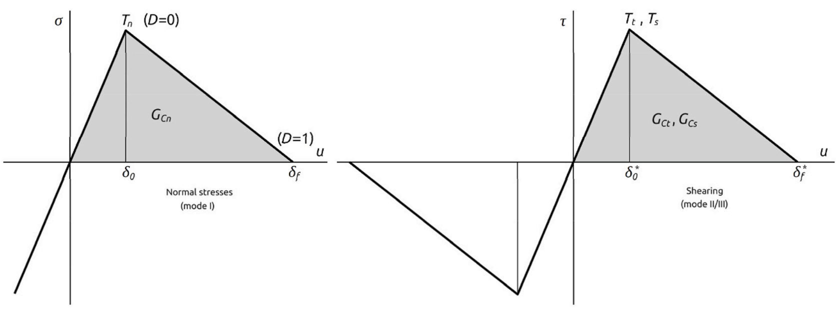

Fig. 6. The traction-separation law for cohesive layer damage formulation.

$$\max\langle\frac{\sigma}{T_{\mathrm{n}}},\frac{\tau_{\mathrm{s}}}{T_{\mathrm{s}}},\frac{\tau_{\mathrm{t}}}{T_{\mathrm{t}}}\rangle=1. \tag{23}$$

When the maximum nominal stress criterion is fulfilled, damage starts with its status D equal to 0. Damage initiation T_*, expressed as a stress value, defines the starting point of the damage and occurs at a given gap value δ_0, equal to:

$$\delta_0=\frac{T_n}{K_p}\ . \tag{24}$$

For all simulations, we kept following the assumption: $T_{\mathrm{n}}=T_{\mathrm{s}}=T_{\mathrm{t}}$. Its value is was selected so that its maximum value corresponds to the maximum strength of the interphase (up to 900 MPa, see Fig. 5), while the lowest was arbitrarily set at value in the range 50–200 MPa, depending on configuration series. Further damage evolution within the cohesive layer is defined by fracture energy/toughness G_{C} and complete damage of the cohesive layer at $D=1$ occurs at the gap value δ_{f} when the interface fails. The fracture energy in mode I - G_{Cn}, similar to shearing modes II and III (G_{ct} and G_{cs}, respectively), is described as follows:

$$G_{\mathrm{Cn}}=\frac{T_{\mathrm{n}}\cdot\delta_{\mathrm{f}}}{2}=\frac{1}{2}\left[T_{\mathrm{n}}\cdot\delta_0+T_{\mathrm{n}}\cdot\left(\delta_{\mathrm{f}}-\delta_0\right)\right]. \tag{25}$$

This determines the evolution of the cohesive zone damage. A low, near-zero value of the fracture energy causes the degradation process to be sudden, while a considerable value extends the damage process. Typical fracture energy for sintered composite materials varies significantly depending of interface type [51,78]. During our calculations, we used fracture energy within the range 0.005–5 J/m^2 to describe rather brittle ceramics/metal interface behaviour and its impact on the macroscopic properties of the composite.

4. Numerical results

4.1. General overview

Based on the methodology introduced in Section 3, we present a comprehensive investigation of the impact of interphase plasticity and ductility (Section 4.3), and interfacial cohesive properties (Section 4.4) on the effective mechanical behaviour of a unit-cell model of a composite comprising metal matrix (nickel), ceramic particle reinforcement (silicon carbide) and interphase in the in-between position. As expected, the various interphase properties applied in the EPD model as the input brought altered fracture modes.

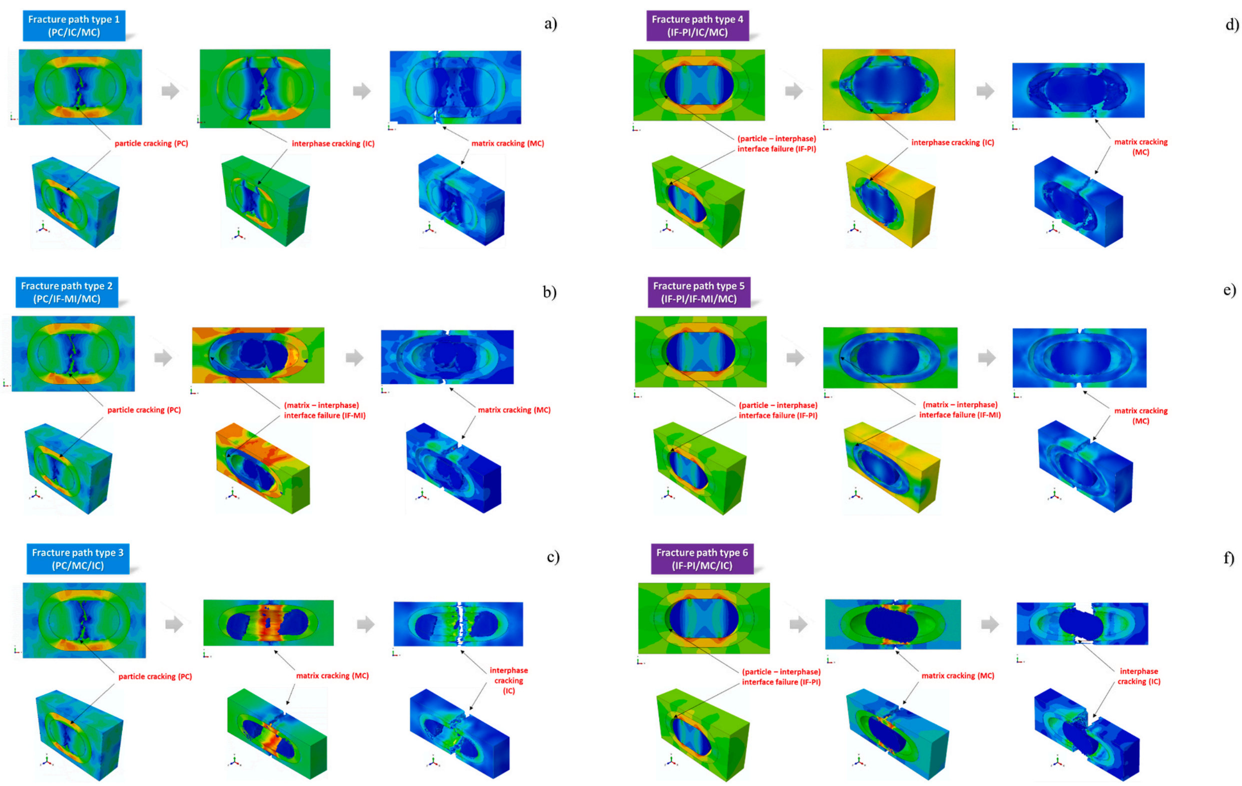

Fig. 7. Various types of fracture modes registered from the FEM simulations of composites with different mechanical properties of interphase and interfaces.

Fig. 7 reveals six main damage types, with specific descriptions of single fracture events. The obtained damage types, together with effective stress-strain curves and macroscopic quantities of composites (Table 4), are discussed in the following sections.

4.2. Calibration of the Gurson-Tvergaard-Needleman model of the metal matrix

The first step of the numerical analysis was obtaining the most realistic data on the mechanical properties of the primary composite components: the metal matrix and ceramic particles. In the first case, we performed the numerical calibration procedure by fitting the elastic, plastic and damage parameters to experimental data from the uniaxial tensile test of a pure nickel sample.

The spark plasma sintering technique was employed to fabricate nickel samples [5,6]; their relative density (ρ_{rel}) was calculated as 97.2 % using the hydrostatic method based on Archimedes' principle. Tensile tests were performed at room temperature using a universal Zwick Roell Z005 testing machine, equipped with a 1 kN force transducer. The experiments were conducted under displacement control at a strain rate of 10^{-3} s^{-1}. Specimens with a gauge length of 5 mm and a cross-sectional area of 0.6 × 0.8 mm were utilised. Strain measurements were obtained through Digital Image Correlation. The stress-strain curve of the uniaxial tension test of representative pure nickel sample is shown in Fig. 8.

The material shows typical ductile behaviour with large plastic deformation, significant strengthening, and rapid softening just before failure, which occurs above 40 % strain [6]. Considering the residual porosity of the sintered Ni sample (~3 %), we assumed the material to be a porous elastoplastic one supplemented by a failure mechanism. GTN model parameters were attuned to reproduce the experimental load curve. Elastic parameters of metallic nickel (Young's modulus E, Poisson's ratio ν) and its theoretical density were adopted from the literature (Table 2). Experimental measurements suggest that the yield stress of a sintered nickel sample will be approximately 155 MPa, with hardening during the tensile test, up to the ultimate tensile strength $\sigma_{UTS} = 375$ MPa at ultimate elongation, $\varepsilon_u = 0.35$. In order to model the most appropriate plastic hardening, analytically, we assumed the Swift model (Eq. (23)) and tuned its parameters to obtain consistency between the analytical and experimental approaches. Finally, based on the GTN model, there is satisfactory correspondence for the elastoplastic deformation range with the final damage (Fig. 8), using the input parameters shown in Tables 2 and 3. The GTN model, based on the porosity effect, reduces stress hardening significantly, mainly by the initial porosity parameter ($f_0 = 0.028$) and its further evolution up until the final porosity f_F, at which the sample fails (in our case $f_F = 0.16$).

4.3. The effect of interphase plasticity and ductility

Having calibrated the elastoplastic properties of the nickel matrix and assumed brittle properties for the silicon carbide particle, numerical simulations of the uniaxial tensile test were performed for a three-phase composite model. In this stage of the calculations, we assumed ideal (perfect) interfaces (i.e. no cohesive elements) with coherent transitions between composite layers. This means that the macroscopic properties of the composite only depend on the properties of the separated composite phases.

The primary objective of this computational study was to investigate the impact of different plastic types of interphase (I_1-I_4) on the effective mechanical properties of the composite. The designed composites were divided into three groups, related to the deformation/damage interphase character indicated by its failure strain: brittle ($\varepsilon_f^{pl} = 0.01$), semi-ductile ($\varepsilon_f^{pl} = 0.1$), or ductile ($\varepsilon_f^{pl} = 0.3$). A comprehensive characterisation of the plasticity and ductility assigned to the interphases is presented in Fig. 5, with variations in yield stress, the nature of the hardening behaviour, and the failure strain. The macroscopic quantities (UTS, ductility, toughness) determined from FE simulations are shown in Table 4. The results of the numerical simulations are illustrated in Figs. 9–14.

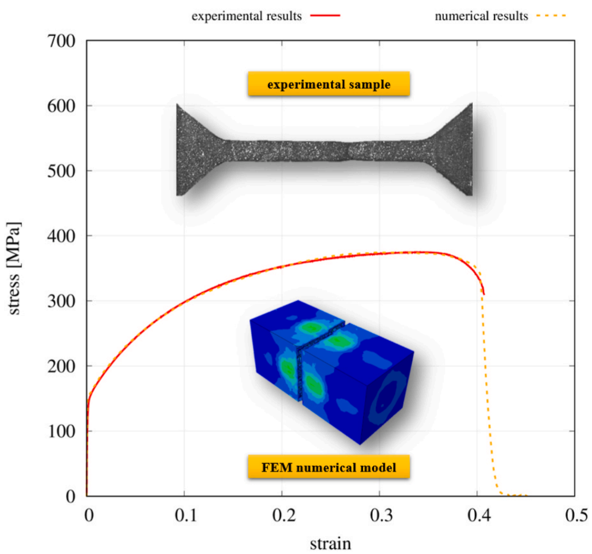

Fig. 8. The calibration of the GTN model of a pure nickel sample with the experimental results from uniaxial tensile tests.

Table 2
Elastic and plastic properties of FE simulations of tensile test of pure nickel sample.

Young's modulus E [GPa]	Poisson's ratio ν	Yield stress σ_y [MPa]	Theoretical density ρ_t [kg/m^3]	Strength coefficient K [MPa]	Strain hardening exponent n [−]	Initial strain ε_0
175	0.31	155	8900	960	0.47	0.022

Table 3
GTN model parameters of FE simulations of tensile test of pure nickel sample.

q_1	q_2	q_3	ε_n	S_n	f_n	f_C	f_F	f_0
1.5	1	2.25	0.3	0.1	0.0065	0.03	0.16	0.028

Table 4
Macroscopic results from FE simulations of a unit-cell model of composites with interphase.

Samples			**Ultimate Tensile Strength [MPa]**	**Ductility [%]**	**Toughness [MJ/m^3]**
Pure nickel			374.6	41.3	132.2
Interphase failure strain, ε_f^{pl} = **0.01**	Ni-SiC with **brittle** interphase	Interphase I_1	200.2	17.4	29.2
		Interphase I_2	200.2	17.4	29.2
		Interphase I_3	209.9	12.2	20.4
		Interphase I_4	209.9	12.5	20.9
Interphase failure strain, ε_f^{pl} = **0.1**	Ni-SiC with **semi-ductile** interphase	Interphase I_1	254.5	22.5	50.0
		Interphase I_2	285.4	24.4	59.8
		Interphase I_3	299.9	24.0	63.6
		Interphase I_4	325.1	25.2	71.1
Interphase failure strain, ε_f^{pl} = **0.3**	Ni-SiC with **ductile** interphase	Interphase I_1	294.6	38.6	88.4
		Interphase I_2	348.9	49.8	144.3
		Interphase I_3	339.4	39.6	121.3
		Interphase I_4	348.6	25.8	76.3

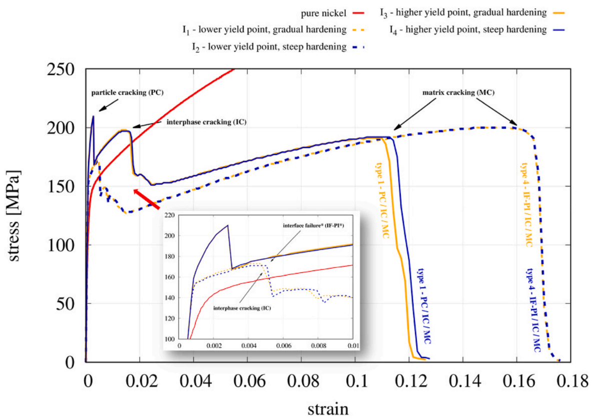

Fig. 9. The stress-strain evolution of composite samples with different plastic types of interphases (I_1-I_4) characterised by **brittle** deformation/damage (interphase failure strain ε_f^{pl}, = **0.01**).

4.3.1. The effect of brittle interphase

The first analysis considered composites with brittle interphase with relatively sudden damage expressed by a failure strain equal to 1 % (Fig. 9). The evolution of effective (macroscopic) stress-strain has been plotted for each composite type. Several characteristic points on the curves can be specified. The initial deformation, with the sharp growth of stress, is common for all composite configurations, and is associated with the highly elastic properties of ceramic particles and the interphase (Table 1). Furthermore, a sudden drop in stress, related to initial material failure, should be noted. The detailed characterisation of the fracture of single parts (particle and interphase), with the content of damaged elements (red), along with deformation, is shown in Fig. 10. Due to the type of fracture mode (and the stress-strain characteristics), the curves can be split into two groups depending on their yield point. Composites with interphase characterised by gradual and steep hardening curves for different yield stresses are identical (means $I_1 \approx I_2$ and $I_3 \approx I_4$) due to the fact that their failure strain is too low for plastic hardening to make a difference. Therefore, the evolution of damaged parts has only been shown for materials with I_1 and I_3 interphases.

Two different fracture modes were detected in the ceramic particle at the very beginning of the simulations. Composites with interphase types I_3 and I_4 break along the particle with a crack path developed perpendicular to the loading direction (see image F1 in Fig. 10), irrespective of the character of the hardening curve (gradual or steep). Moreover, the 'skinning effect' can be observed and is manifested by sudden damage of the finite elements located in the contact surface of the particle and interphase. These two damage effects (particle breakage and skinning effect) have a dynamic character, erasing more than 30 % of the particle elements.

Significantly altered damage behaviour in the ceramic phase can be found in the composite with the I_1/I_2 interphase type. Lower yield stress in the interphase leads to localised damage close to the interface of the particles and the interphase (see F2 in Fig. 10). Only a low percentage of particle elements are damaged and removed at the bonding surface, positioned perpendicular to the loading direction. The presented fracture mode can be defined as particle-interphase interface failure, localised in the spherical part of the interphase (denoted as *IF(PI)**), despite the assumption of perfect element bonding. The observed interface failure resembles interface delamination due to breakage/damage of the cohesive elements at the interface; this is discussed in section 4.4.

Together with the failure of the interface between the particle and interphase, simultaneously, the degradation of the interphase can be seen ($\varepsilon = 0.005$) due to the cracking (a sudden drop of damaged elements) and the subsequent gradual skinning effect (see F4 in Fig. 10). It should be pointed out that the final reduction of the active finite elements, due to damage (in red) is close to 50 %. Despite this fact, the overall effective failure strain of the composite with I_1/I_2 interphase type exceeds 0.165, while that for I_3/I_4 type only reaches 0.11. However, the level of degradation of interphase I_3/I_4 is about half the size (≈22 %). This can be explained by the magnitude/degree of connection between the brittle interphase and the matrix. As the interphase I_1/I_2 loses its bonding with the matrix, due to the considerable skinning effect, it does not participate in the load/stress transfer, allowing the pure nickel matrix to elongate to the final fracture without any restrictions from the brittle part (interphase). Interphase I_3/I_4 keeps the bonding with the ductile matrix, increasing the internal stresses and reducing the macroscopic toughness of the system, leading to relatively premature failures by the matrix cracking (MC) fracture mode.

4.3.2. The effect of semi-ductile interphase

As expected, an increase of the failure strain of the interphase (to 0.1) leads to more privileged macroscopic results (Fig. 11): there is a higher ultimate tensile strength, more profound ductility and toughness, compared to previously investigated composites with brittle interphase (Fig. 9). Furthermore, it was found that composites with semi-ductile interphase are subjected to the same type of fracture, regardless of the type of the interphase's plastic behaviour (I_1-I_4). The application of higher ε_f^{pl} of interphase leads to the occurrence of one type of fracture mode (the type 1 – PC/IC/MC), while lower $\varepsilon_f^{pl} = 0.01$ brought two types: type 1 and type 4 – IF(PI)*/IC/MC. The

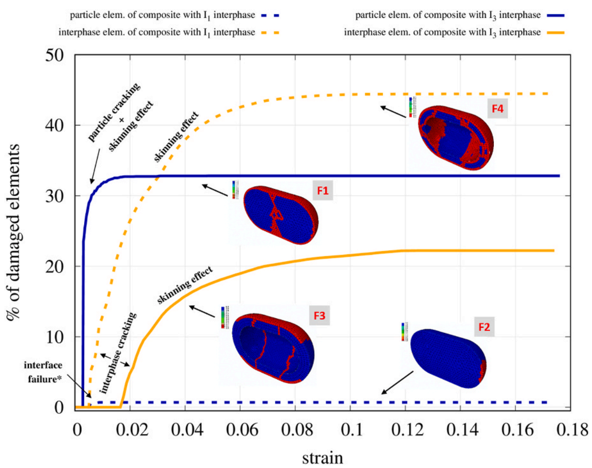

Fig. 10. The evolution of damaged elements (marked in red) of particle and interphase parts of composite samples with different plastic types of interphases (I_1~I_2 and I_3~I_4), characterised by **ductile** deformation/damage (interphase failure strain, $\varepsilon_f^{pl} = \mathbf{0.01}$).

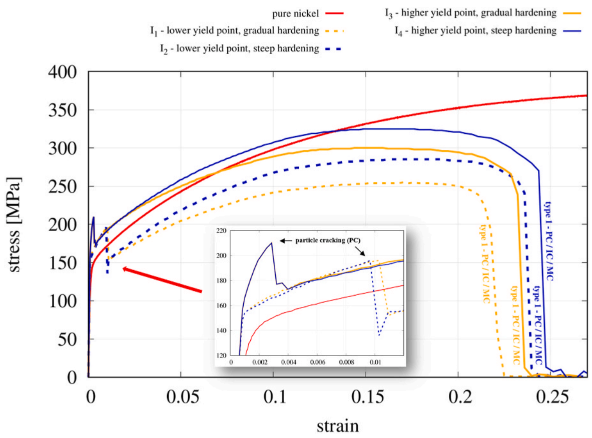

Fig. 11. The stress-strain evolution of composite samples with different plastic types of interphases (I_1-I_4) characterised by **semi-ductile** deformation/damage (interphase failure strain, $\varepsilon_f^{pl} = \mathbf{0.1}$).

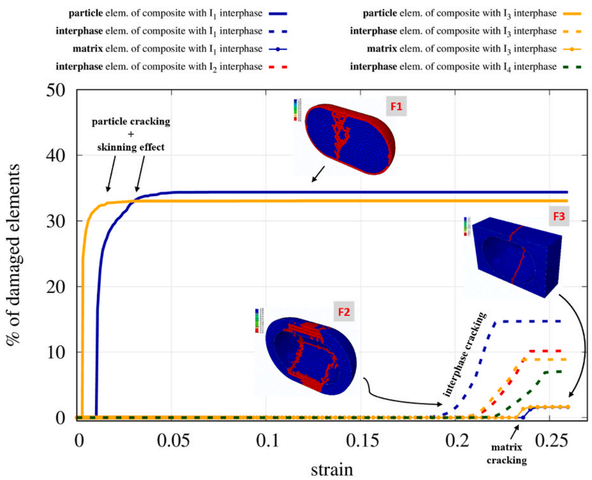

Fig. 12. The evolution of damaged elements of particle, interphase and matrix parts of composite samples with different plastic types of interphases (I_1-I_4), characterised by **ductile** deformation/damage (interphase failure strain, $\varepsilon_f^{pl} = \mathbf{0.1}$).

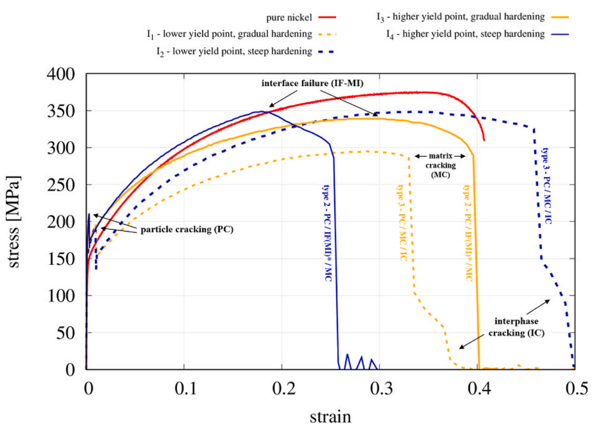

Fig. 13. The stress-strain evolution of composite samples with different plastic types of interphases (I_1-I_4), characterised by **ductile** deformation/damage (interphase failure strain, $\varepsilon_f^{pl} = \mathbf{0.3}$).

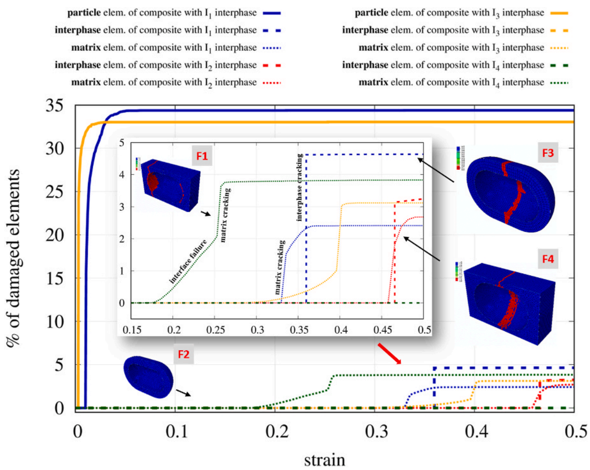

Fig. 14. The evolution of damaged elements of particle, interphase and matrix parts of composite samples with different plastic types of interphases (I_1-I_4), characterised by **ductile** deformation/damage (interphase failure strain, $\varepsilon_f^{pl} = \mathbf{0.3}$).

assumed semi-ductile character of the interphase causes the composite to start to degrade by particle cracking, with mechanisms comparable to the example with extremely brittle interphase, i.e. cracking along the particle with a skinning effect (see F1 in Fig. 12). Composites with the I_3/I_4 interphase initiate this a little bit sooner, probably due to the higher yield point applied, which accelerates the critical stress to failure.

Finally, the four simulations brought various macroscopic mechanical responses and deviated from each other; thus, we cannot group them because of the effect of the plastic hardening curve type. The semi-ductile evolution type of stress-strain curves is governed by the plastic properties of the interphase, in which the steep hardening seems to be the most crucial applied parameter, giving the largest ductility. As shown in Fig. 12, the lower yield point (I_1/I_2) causes earlier interphase cracking of a non-trivial character (see image F2) with breakage localised in the geometry transition area, where the spherical part of the particle is reshaped to a cylindrical one, together with rupturing oriented parallel to the direction of loading. Finally, some elements were damaged at the interphase region. The fracture of interphase occurs relatively close to the matrix fracture (with respect to time or the deformation's progress); hence, for single composite models (I_3), the failure of interphase and matrix (see F3 in Fig. 12) may overlap/happen close together, giving the gradual drop of macroscopic stress in the ductile softening curve (especially composites with I_3/I_4 interphase, see Fig. 11).

4.3.3. The effect of ductile interphase

The final composite type considered was the one with ductile interphase characterised by failure strain, $\varepsilon_f^{pl} = 0.3$ (Fig. 13). Progressive improvement in the effective plastic properties (comparable to the pure nickel) was observed and, in one case, was even more advantageous (the composite with I_2 interphase). However, the UTS of such materials is still reduced, compared to nickel. Compared to composites with lower ε_f^{pl}, we observed the transition of fracture modes. Here, two new fracture modes can be specified: type 2 – PC/IF (MI)*/MC and type 3 - PC/MC/IC, for materials with the higher (I_3/I_4) and lower yield point (I_1/I_2) of interphase, respectively.

In the first case (I_3/I_4), there may be interface failure on the contact zone between the matrix and the interface (see F1 in Fig. 14), which leads to sudden matrix cracking. This occurs earlier in the case of the composite with I_4 interphase, mainly due to the applied steep hardening curve, which induces a higher level of stress being transferred to the matrix. Simultaneously, it should be noted that, at the end of the simulation, the interphase part remained undamaged/unfractured (see F2 in Fig. 14). The damage behaviour of the composite with I_1/I_2 interphase is quite different because the interphase cracks in a direction perpendicular to loading (see F3 in Fig. 14) but just after matrix degradation. The matrix of such composites indicates damage characteristics similar to those of the interphase (see F4 in Fig. 14).

4.4. The effect of cohesive interface behaviour

The final stage of the current numerical investigation revealed the severe impact of interfaces between the phases (metal matrix – interphase and interphase – ceramic particle) on the effective mechanical properties of the composite and fracture/damage modes. The mechanical behaviour of the interface was modelled using the cohesive zone model, as described in Section 3.4.

The numerical investigation of the mechanical properties of the composite with imperfect interfaces was performed using the example of two composites with altered states of interphase. The first case considered the material with a brittle interphase I_4, characterised by a high yield point, steep hardening, and relatively fast damage; the second concerned the opposite state, i.e. low yield point, gradual hardening, and slow damage (I_1 interphase). The results for pure nickel and composites with perfect cohesion have been added to complement this study.

Numerical analysis consists of multiple simulations using varied interfacial properties as input: cohesive interfacial strength T_n and fracture energy G_c. Each input parameter was studied for two scenarios; the first assumes the identical properties of both interfaces, and the second presents the results for different properties: particle–interphase (denoted as I) and interphase–matrix (denoted as II).

4.4.1. The effect of cohesive interfacial strength

4.4.1.1. Composites with brittle interphase. Fig. 15 demonstrates the impact of T_n strength (where $T_n = T_s = T_t$) on the stress-strain curves for two different composite materials: brittle (a, c) and ductile (b, d). The first interesting effect can be seen in Fig. 15a, the case of composite with brittle interphase with identical interfaces. The composite with cohesive interface strength of 100 MPa exposed the most considerable toughness and ductility with the highest ultimate tensile strength, even more profound than the one with perfect cohesion. This is surprising, since the higher T_n should guarantee more advantageous global properties. The samples with T_n in the range 500–700 MPa and a perfectly bonded composite showed such a dependence: the higher the cohesive strength, the higher the toughness/ductility obtained. Moreover, all those samples fractured in an identical manner: PC/IC/MC (particle cracking - > interphase cracking - > matrix cracking). Fig. 16a demonstrates the damage evolution of finite elements of the interphase and particle body during the uniaxial tensile simulation.

At the initial deformation stage, the particle fractures perpendicular to the tension direction for samples with the highest cohesion strength, which was evidenced by the sudden increase in the number of damaged elements. As the strain progressed, a skinning effect occurred, as illustrated by the gradual fracture of particle and interphase boundary elements shown in the flatter curve. It was found that over 20 % of the elements were finally damaged in the cases of samples with high cohesion strength. It can be concluded that the skinning effect significantly influences the composite's effective properties, increasing the role of the plastic matrix, which reduces composite brittleness and leads to excellent ductility. The stronger the interface, the more load can be carried by other composite components, stabilising the matrix. Furthermore, a stronger interface prevents voids that could act as failure initiators.

Against this background, the sample with $T_n = 100$ MPa differs significantly. Firstly, compared to samples with the most advantageous cohesion, it breaks in the altered manner by interface failure modes (specifically Type 5), which can be observed in Fig. 16b. Two interfaces detach simultaneously, reducing the overall stiffness and brittleness of the system, and resulting in the highest fracture strain.

Finally, a sample with intermediate cohesion strength ($T_n = 300$ MPa) indicates a mixed fracture mode, as shown in Fig. 16a and b.

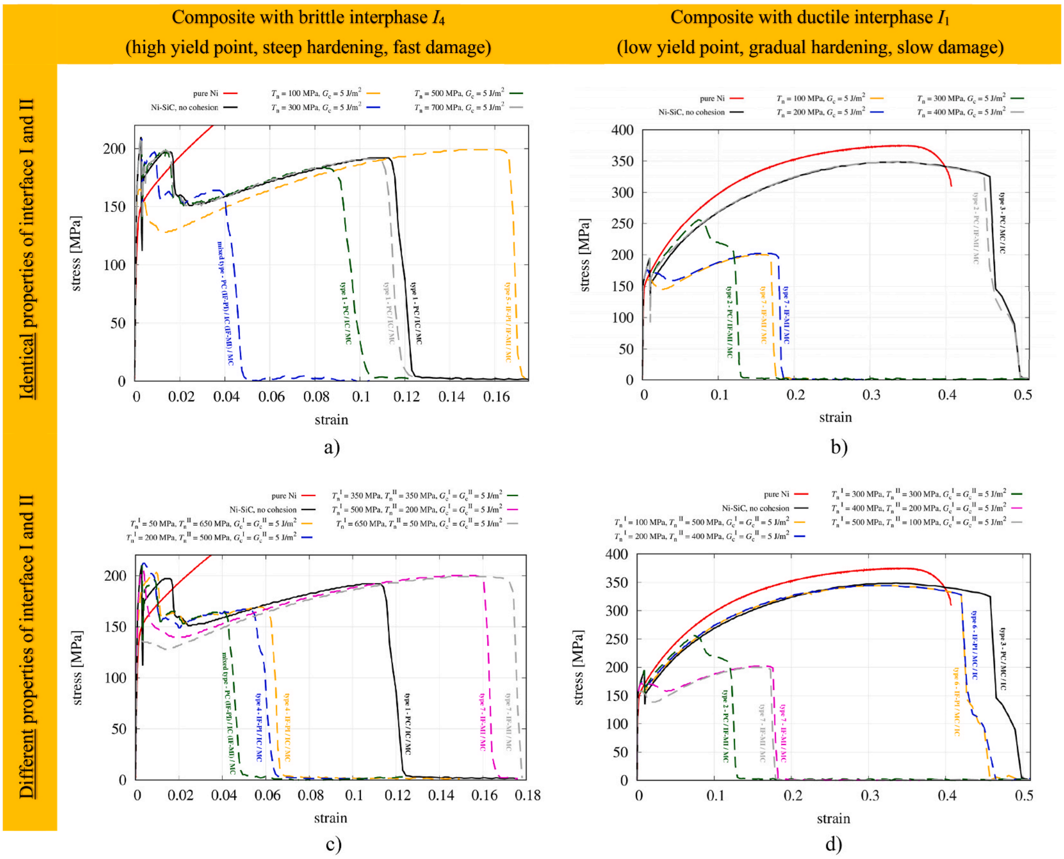

Fig. 15. Stress-strain characteristics of composite samples with brittle I_4 (**a**,**c**) and ductile I_1 (**b**,**d**) interphase with various cohesive strengths of two identical (**a**,**b**) and different (**c**,**d**) interfaces of particle–interphase (denoted as I) and interphase–matrix (denoted as II).

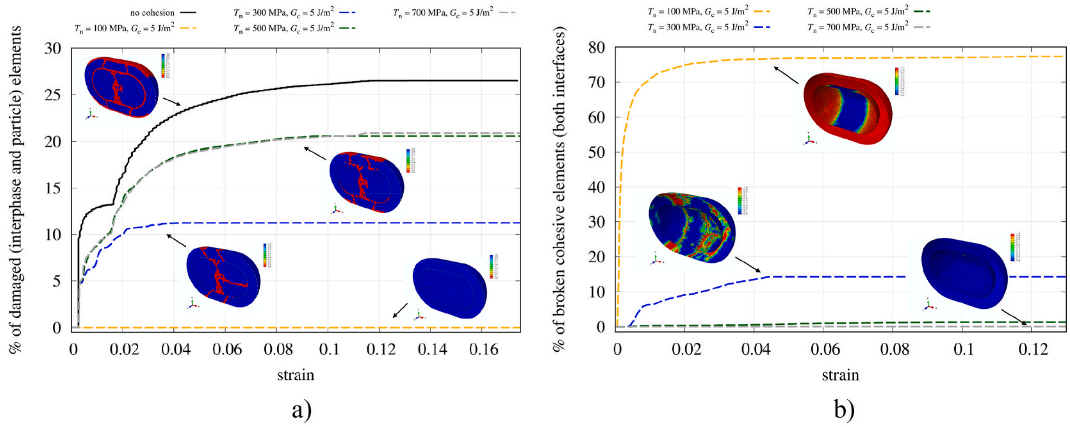

Fig. 16. Detailed analysis of fracture behaviour of composite with **brittle** interphase (I_4) with varying T_n – the evolution of damaged finite elements (a) and broken cohesive elements D (b).

The particle fractures transversely (parallel to the direction of loading) with partial damage to the cohesive elements but without a skinning effect. Interfaces disintegrate near the transition from the spherical to cylindrical shape, causing a crushed particle, with the interphase remaining attached, despite the localised cracks. Such an effect maintains the local material's brittleness. Rapid debonding of the interface part causes stress localisation, leading to the breakage of finite elements near the disintegration. This mechanism makes the sample with intermediate cohesion the weakest of all the materials considered.

Composites with different interfacial properties indicate similar mechanical tendencies to those with identical ones, as shown in Fig. 15c and d. Firstly, regarding the composites with brittle interphases, a weakened interface leads to higher ductility and breaks of fracture mode type 7 (IF-MI/MC), which is a simplified version of type 5 (IF-PI/IF-MI/MC). A considerable resemblance between the curve corresponding to the weakened interface ($T_n = 100$ MPa - orange line in Fig. 15a) and another corresponding to the weakened interface II ($T_n^{II} = 50/200$ MPa - magenta/grey line in Fig. 15c) was observed. The conclusion is that the cohesion of interface II (interphase - matrix) seems to be crucial for beneficial elongation. Low interface strength leads to the detachment of the brittle interphase, together with brittle particles at the initial loading stage, guaranteeing better ductility. In turn, the poor strength of interface I (between particle and interphase – the blue/orange curves in Fig. 15c) changes the fracture mode and reduces effective ductility and UTS.

4.4.1.2. Composites with ductile interphase. The study regarding the composites with brittle interphase demonstrated the occurrence of five different fracture/damage modes (types 1, 4, 5, 7, and mixed) with varying interfacial cohesion strength T_n. In turn, those with ductile interphases indicate four types (type 2 – PC/IF-MI/MC, type 3 – PC/MC/IC, type 6 – IF(PI)/MC/IC and type 7 – IF-MI/MC), see Fig. 15b. Here, the least privileged cohesion conditions ($T_n = 100$ MPa and $T_n = 200$ MPa) brought quite a sudden interface failure between the interphase and matrix, keeping the ceramic particle in an undamaged form (Fig. 15b). It was observed that there is a profound resemblance between the stress-strain curves of the composites and the brittle (I_4) and ductile (I_1) interphases with $T_n = 100$ MPa and $G_c = 5$ J/m^2 (the orange lines in Fig. 15a and b). This leads to the conclusion that the interphase properties became irrelevant, in the context of effective behaviour, when there was complete failure of interface I (particle-interphase) and no particle cracking effect. Moreover, a slight change in fracture mode was noticed: brittle – type 5 and ductile – type 7. The latter became a modification to type 5, without interfacial failure between the particle and interface.

Increasing the cohesive strength to 300 MPa (and above) ensured an altered fracture mode, by adding particle cracking. Such a feature allows the composites to obtain higher ultimate tensile strength; however, the failure strain drops. Once again, it was proved that residues of the brittle particle part lead to less privileged ductility when we compared the cases with $T_n = 100/200$ MPa and 300 MPa. Finally, the most beneficial cohesive properties ($T_n = 400$ MPa) ensured a considerable effective response (highest ductility and toughness), similar to the one with perfect conditions, with only minor differences in fracture mode (the composite with perfect cohesion – type 3 and where $T_n = 400$ MPa – type 2).

Diverse interface properties in the composite, when a ductile interphase is assumed, do not significantly affect the effective composite (Fig. 16d). By comparing composites with identical and altered interfacial properties, we can observe the significant similarities of each case, i.e. identical interfaces with $T_n = 100/200$ MPa (orange and blue curves in Fig. 15b) and the altered one, where interface II - $T_n^{II} = 100/200$ MPa (grey/magenta curve in Fig. 15d). Such an effect was also noticed for the composite with brittle interphase. It can be confirmed that interface II (between the matrix and interphase) significantly governs the macroscopic composite's performance.

4.4.2. The effect of fracture energy

Let us now consider the complex impact of the fracture energy of the interface G_c on the macroscopic response; see Fig. 17a and c (brittle composite), and 17b and 17d (ductile composite). For each of the two cases, we varied the G_c value for two sets of T_n: for the brittle composite, we chose $T_n = 350$ and 700 MPa; and, for the ductile composite, $T_n = 300$ and 400 MPa. The choice of such specific values of T_n was not arbitrary; it revealed a broad palette of dependence of G_c on strength, ductility, and toughness.

4.4.2.1. Composites with brittle interphase. As was shown in a subsection 4.4.1. (regarding the effect of varying T_n), the most advantageous cohesive properties (with relatively high strength $T_n = 700$ MPa) brought the effective properties close to those with perfect cohesion. Here, assuming that $T_n = 700$ MPa, the application of lower values of G_c did not significantly affect the composite properties. As shown in Fig. 17a (identical interfacial properties), there is slightly less ductility with only minor differences, whilst keeping an identical fracture mode (type 1) without any damage caused by interface failure (Fig. 18b).

The opposite dependence can be noted for $T_n = 350$ MPa. A relatively low cohesive strength ($T_n = 350$ MPa) and high fracture energy ($G_c = 5$ J/m^2 – acting as the weak and ductile bonding with a substantial softening range) seems to be the most disadvantageous combination of cohesive properties, in the context of effective properties. It causes progressive damage to cohesive elements (∼10 %, see Fig. 18b), which is not prominent enough to significantly separate the two contacting bodies but large enough to produce local defects at the interface. It initiates interphase rupture, resulting in the lowest effective ductility and toughness (Fig. 17a). The decrease in G_c slightly enhances the composite properties and changes the fracture mode to mix one. Once more, it was confirmed that weakening the interface between brittle particle and interphase (and/or brittle interphase and matrix) degrades most of the cohesive elements (Fig. 18b), which causes more load to be carried by the matrix. Hence, it limits finite element damage (Fig. 18a), allowing more extended elongation (Fig. 17a). The broken bonds appear progressively, starting with interface failure between the particles and interphase, leading to fracture between the matrix and interphase (Fig. 18b).

Altering the fracture energy ($G_c^I, G_c^{II} \in \{0.05, 0.5, 5\}$ J/m^2) of two studied interfaces, while keeping their strength equal ($T_n^{\mathrm{I}}, T_n^{\mathrm{II}} =$ 350 MPa), lead to similar results as for the homogeneous ones. The considerable effects of changing fracture modes or increasing/decreasing macroscopic performance were observed (Fig. 17c). All of the fracture energy combinations within the composite interfaces indicate mixed-type fracture modes.

On the other hand, the composites differ by a percentage (%) of the final damage to the interphase part. Increasing the ratio G_c^I/G_c^{II} drops the damaged finite elements of the interphase from ∼10 % (for $G_c^I/G_c^{II} = 10^{-4}$) to ∼4 % (for $G_c^I/G_c^{II} = 10^4$). Hence, by making the interface of the particle-interphase more ductile (by increasing its fracture energy), we better prevent the interphase part from degrading. Simultaneously, the percentage of final damage of the particle part remains at a similar level (∼11 %) as changing the ratio

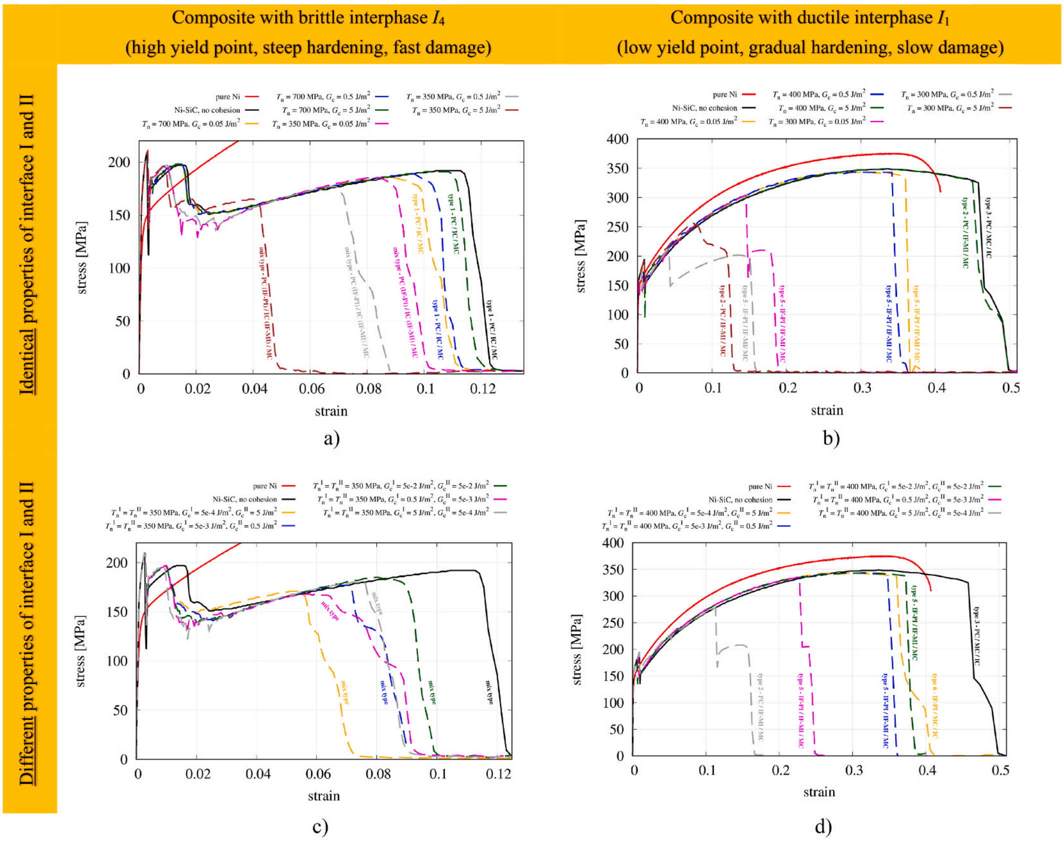

Fig. 17. Stress-strain evolution of composite with brittle I_4 (**a**,**c**) and ductile I_1 (**b**,**d**) interphase with various fracture energies of two identical (**a**,**b**) and different (**c**,**d**) interfaces of particle–interphase (denoted as I) and interphase–matrix (denoted as II).

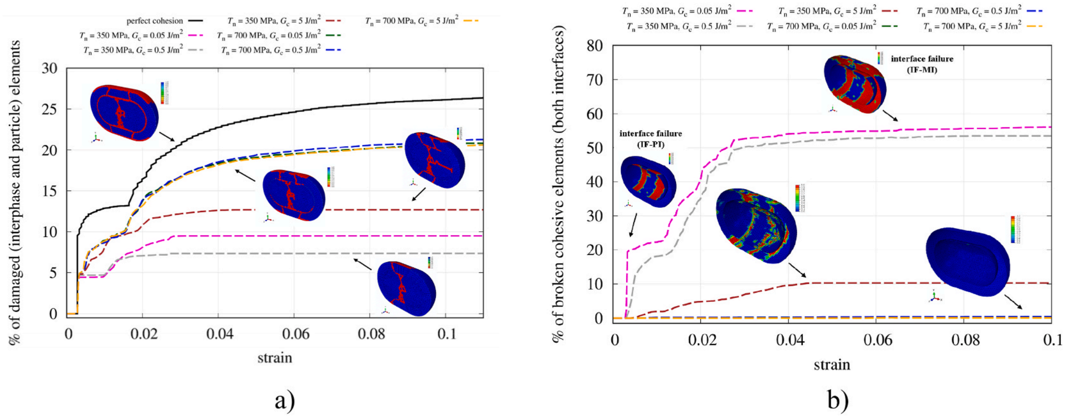

Fig. 18. Detailed analysis of fracture behaviour of the composite with **brittle** interphase (I_4) with varying G_c – the evolution of damaged finite elements (a) and broken cohesive elements D (b).

G_c^I/G_c^{II}.

4.4.2.2. Composites with ductile interphase. By having both interfaces with a higher T_n (400 MPa), the reduction of G_c energy leads to more brittle characteristics of the interfaces, which switches the fracture mode from type 2 to 5, by replacing the particle cracking (G_c = 5 J/m^2) to interface failure between the particles and interphase ($G_c \in \{0.05, 0.5\}$ J/m^2). The modification allows us to obtain satisfactory effective ductility (Fig. 17b); however, it is less privileged than the reference composite (T_n = 400 MPa, G_c = 5 J/m^2). Analogous G_c reduction, whilst keeping lower interfacial strength (T_n = 300 MPa) reveals similar dependence-change fracture modes; it simultaneously improves effective ductility in the reference case (T_n = 300 MPa, G_c = 5 J/m^2). Moreover, applying G_c = 0.05 J/m^2 enhances UTS and toughness.

Finally, considering the different ductility (fracture energy) of interface I (particle-interphase) and II (matrix-interphase) reveals three fracture modes (Fig. 17d). It should be restated that interface II governs the macroscopic properties of composites and reduces them, as we decrease G_c^{II}. As stated in the previous paragraph, T_n^{II} also decreases (Fig. 15d). The drop of G_c^{II} (from $5 \cdot 10^{-4}$ to $5 \cdot 10^0$ J/m^2) leads to the degradation of composite ductility, from ∼40 % to ∼10 %. The fracture energy of interface I affects the global response slightly; however, for the lowest value, $G_c^I = 5 \cdot 10^{-4}$ J/m^2, the fracture modes are swift.

5. Concluding remarks

The presented work can be summarised as follows.

1. A finite element framework was employed to investigate the impact of various properties of the interphase zone on the effective mechanical properties of multiphase composite material. Three constitutive material models were employed to predict the deformation and damage to the main composite components (metal matrix, interphase, ceramic particles, and interfaces): the Gurson–Tvergaard–Needleman, an elastic-plastic model with damage, and a cohesive zone model.
2. The wide range of interphase properties was simulated, from brittle ones with a less plastic character (similar to ceramic particle properties) to ductile ones with a yield point, hardening, and failure strain close to the metal matrix. The effect of cohesive parameters (cohesive strength and fracture energy) of the interfaces (particle-interphase and matrix-interphase) was studied.
3. More than six fracture modes were registered during the uniaxial tensile test simulations of the unit-cell model. Most cases revealed particle cracking as the first fracture mechanism. Moreover, as the perfect cohesion of interfaces was assumed, the skinning effect, related to damage evolution within finite elements located near the interface between ceramic particles and interphase, was observed and played a significant role in fracture damage.
4. The considerable impact of interphase brittleness on effective composite properties was shown. The highly brittle interphase with failure strain equal to 0.01 reduced the composite ductility. However, by assuming a lower yield point, we may preserve the elongation of the composite at a value of approximately 18 %. Ductile interphase, with a failure strain equal to 0.3, brought about significant elongation; in some cases, up to 50 % (lower yield point, steep hardening curve), which more than exceeded that for pure nickel (∼40 %).
5. The most beneficial cohesive parameters, such as high cohesive strength (700 MPa) and fracture energy (5 J/m^2), allowed us to duplicate the mechanical performance of the composite corresponding to the perfect bonding between its components. However, the significant decrease of interface strength (to 100 MPa) in the brittle-type composite lead to the complete delamination of brittle particle and interphase from the ductile matrix, enhancing the overall ductility and toughness. The least favourable effective properties indicated a composite with intermediate cohesive strength (around 300 MPa) causing two parallel fracture modes: particle/interphase cracking together with interface failure.

6. A comparison of the macroscopic behaviour of composites with brittle and ductile interphases demonstrated that the properties of the interphase lose significance when the complete interfacial failure between particle and interphase occurs, accompanied by the absence of particle cracking effects.
7. Numerical simulations confirmed that the interface between the interphase and the matrix is more critical within the composite and plays a significant role in determining the macroscopic performance of both brittle and ductile type composites, mainly affecting ductility and toughness, since the cohesive parameters of the interface between particle and interphase have a minimal impact on the overall response.

CRediT authorship contribution statement

Szymon Nosewicz: Writing – review & editing, Writing – original draft, Validation, Supervision, Project administration, Methodology, Investigation, Funding acquisition, Formal analysis, Conceptualization. **Grzegorz Jurczak:** Visualization, Software, Methodology, Investigation.

Declaration of competing interest

The authors declare that they have no known competing financial interests or personal relationships that could have appeared to influence the work reported in this paper.

Acknowledgements

The authors would like to acknowledge financial support from the National Science Centre, Poland, under Grant Agreement No. OPUS 2020/37/B/ST8/03907 for the project "*Multiscale investigation of deformation and damage behaviour of novel hybrid metal matrix composites. Experimental studies and numerical modelling*", and No. OPUS 2023/49/B/ST8/04228 for the project "*Tailoring mechanical properties of metal matrix composites by controlling reinforcing particles distribution.*"

Data availability

Data will be made available on request.

References

[1] O. Elmhaia, O. Askour, Y. Sitli, S. Mesmoudi, M. Rammane, O. Bourihane, et al., Investigation of nonlinear buckling of FGM shells using a high-order finite continuation approach, Finite Elem. Anal. Des. 242 (2024) 104273, https://doi.org/10.1016/j.finel.2024.104273.
[2] X. Guo, D. Tian, C. Li, X. Li, W. Li, M. Cao, et al., Optimization for the process parameters of nickel–titanium Nitride composites fabricated via Jet Pulse electrodeposition, Nanomaterials 14 (2024) 2034, https://doi.org/10.3390/nano14242034.
[3] J.J. Zhao Yuhong, Current research status of interface of ceramic-metal laminated composite material for armor protection, Acta Metall. Sin. 57 (2021) 1107–1125, https://doi.org/10.11900/0412.1961.2021.00051.
[4] T. Fan, Z. Ruan, F. Zhong, C. Xie, X. Li, D. Chen, et al., Nucleation and growth of L12-Al3RE particles in aluminum alloys: a first-principles study, J. Rare Earths 41 (2023) 1116–1126, https://doi.org/10.1016/j.jre.2022.05.018.
[5] M. Chmielewski, R. Zybała, A. Strojny-Nędza, A. Piątkowska, A. Dobrowolski, J. Jagiełło, et al., Microstructural evolution of Ni-SiC composites manufactured by spark plasma sintering, Metall. Mater. Trans. A 54 (2023) 2191–2207, https://doi.org/10.1007/s11661-023-06999-w.
[6] S. Nosewicz, P. Jenczyk, B. Romelczyk-Baishya, P. Bazarnik, D. Jarząbek, K. Majchrowicz, et al., The influence of spark plasma sintering on multiscale mechanical properties of nickel-based composite materials, Mater. Sci. Eng., A 891 (2024) 146001, https://doi.org/10.1016/j.msea.2023.146001.
[7] K. Livanov, L. Yang, A. Nissenbaum, H.D. Wagner, Interphase tuning for stronger and tougher composites, Sci. Rep. 6 (2016) 26305, https://doi.org/10.1038/srep26305.
[8] D.A. Jesson, J.F. Watts, The interface and interphase in polymer matrix composites: effect on mechanical properties and methods for identification, Polym. Rev. 52 (2012) 321–354, https://doi.org/10.1080/15583724.2012.710288.
[9] S. Huang, B. Wang, L. Yan, Chapter 6 - interphase and interfacial properties of composite materials, in: I.-M. Low, Y. Dong (Eds.), Composite Materials, Elsevier, 2021, pp. 151–177, https://doi.org/10.1016/B978-0-12-820512-9.00020-4.
[10] S. Psakhie, V. Ovcharenko, B. Yu, E. Shilko, S. Astafurov, Y. Ivanov, et al., Influence of features of interphase boundaries on mechanical properties and fracture pattern in metal–ceramic composites, J. Mater. Sci. Technol. 29 (2013) 1025–1034, https://doi.org/10.1016/j.jmst.2013.08.002.
[11] S. Lurie, P. Belov, D. Volkov-Bogorodsky, N. Tuchkova, Interphase layer theory and application in the mechanics of composite materials, J. Mater. Sci. 41 (2006) 6693–6707, https://doi.org/10.1007/s10853-006-0183-8.
[12] Y. Benveniste, A general interface model for a three-dimensional curved thin anisotropic interphase between two anisotropic media, J. Mech. Phys. Solid. 54 (2006) 708–734, https://doi.org/10.1016/j.jmps.2005.10.009.
[13] M.B. Rubin, Y. Benveniste, A Cosserat shell model for interphases in elastic media, J. Mech. Phys. Solid. 52 (2004) 1023–1052, https://doi.org/10.1016/j.jmps.2003.09.030.
[14] N. Chandra, H. Li, C. Shet, H. Ghonem, Some issues in the application of cohesive zone models for metal–ceramic interfaces, Int. J. Solid Struct. 39 (2002) 2827–2855, https://doi.org/10.1016/S0020-7683(02)00149-X.
[15] K. Park, G.H. Paulino, Cohesive zone models: a critical review of traction-separation relationships across fracture surfaces, Appl. Mech. Rev. 64 (2013), https://doi.org/10.1115/1.4023110.
[16] G. Alfano, On the influence of the shape of the interface law on the application of cohesive-zone models, Compos. Sci. Technol. 66 (2006) 723–730, https://doi.org/10.1016/j.compscitech.2004.12.024.
[17] W.X. Zhang, L.X. Li, T.J. Wang, Interphase effect on the strengthening behavior of particle-reinforced metal matrix composites, Comput. Mater. Sci. 41 (2007) 145–155, https://doi.org/10.1016/j.commatsci.2007.03.011.
[18] H. Qing, 2D micromechanical analysis of SiC/Al metal matrix composites under tensile, shear and combined tensile/shear loads, Mater. Des. 51 (2013) 438–447, https://doi.org/10.1016/j.matdes.2013.04.051.
[19] Y. Cheng, L. Bian, Y. Wang, F. Taheri, Influences of reinforcing particle and interface bonding strength on material properties of Mg/nano-particle composites, Int. J. Solid Struct. 51 (2014) 3168–3176, https://doi.org/10.1016/j.ijsolstr.2014.05.007.

[20] S. Ben, J. Zhao, T. Rabczuk, A theoretical analysis of interface debonding for coated sphere with functionally graded interphase, Compos. Struct. 117 (2014) 288–297, https://doi.org/10.1016/j.compstruct.2014.07.004.
[21] A.S. Sarvestani, On the overall elastic moduli of composites with spherical coated fillers, Int. J. Solid Struct. 40 (2003) 7553–7566, https://doi.org/10.1016/S0020-7683(03)00299-3.
[22] Y. Jiang, H. Yang, K. Tohgo, Three-phase incremental damage theory of particulate-reinforced composites with a brittle interphase, Compos. Struct. 93 (2011) 1136–1142, https://doi.org/10.1016/j.compstruct.2010.10.010.
[23] M.P. Lutz, R.W. Zimmerman, Effect of the interphase zone on the conductivity or diffusivity of a particulate composite using Maxwell's homogenization method, Int. J. Eng. Sci. 98 (2016) 51–59, https://doi.org/10.1016/j.ijengsci.2015.07.006.
[24] Y.M. Wu, Z.P. Huang, Y. Zhong, J. Wang, Effective moduli of particle-filled composite with inhomogeneous interphase: Part I – bounds, Compos. Sci. Technol. 64 (2004) 1345–1351, https://doi.org/10.1016/j.compscitech.2003.10.009.
[25] Y. Zhong, J. Wang, Y. Ming Wu, Z.P. Huang, Effective moduli of particle-filled composite with inhomogeneous interphase: Part II – mapping method and evaluation, Compos. Sci. Technol. 64 (2004) 1353–1362, https://doi.org/10.1016/j.compscitech.2003.10.010.
[26] F. Dinzart, H. Sabar, S. Berbenni, Homogenization of multi-phase composites based on a revisited formulation of the multi-coated inclusion problem, Int. J. Eng. Sci. 100 (2016) 136–151, https://doi.org/10.1016/j.ijengsci.2015.12.001.
[27] T. Mori, K. Tanaka, Average stress in matrix and average elastic energy of materials with misfitting inclusions, Acta Metall. 21 (1973) 571–574, https://doi.org/10.1016/0001-6160(73)90064-3.
[28] T. Mura, Micromechanics of Defects in Solids, vol. 3, Springer Netherlands, Dordrecht, 1987, https://doi.org/10.1007/978-94-009-3489-4.
[29] S. Nemat-Nasser, T. Iwakuma, M. Hejazi, On composites with periodic structure, Mech. Mater. 1 (1982) 239–267, https://doi.org/10.1016/0167-6636(82)90017-5.
[30] A. Riccardi, F. Montheillet, A generalized self-consistent method for solids containing randomly oriented spheroidal inclusions, Acta Mech. 133 (1999) 39–56, https://doi.org/10.1007/BF01179009.
[31] P. Joshi, S.H. Upadhyay, Effect of interphase on elastic behavior of multiwalled carbon nanotube reinforced composite, Comput. Mater. Sci. 87 (2014) 267–273, https://doi.org/10.1016/j.commatsci.2014.02.029.
[32] Y.M. Shabana, A micromechanical model for composites containing multi-layered interphases, Compos. Struct. 101 (2013) 265–273, https://doi.org/10.1016/j.compstruct.2013.02.008.
[33] J. Choi, H. Shin, S. Yang, M. Cho, The influence of nanoparticle size on the mechanical properties of polymer nanocomposites and the associated interphase region: a multiscale approach, Compos. Struct. 119 (2015) 365–376, https://doi.org/10.1016/j.compstruct.2014.09.014.
[34] X. Yang, G.Q. Wu, W. Sha, Q.Q. Zhang, Z. Huang, Numerical study of the effects of reinforcement/matrix interphase on stress–strain behavior of YAl2 particle reinforced MgLiAl composites, Compos. Appl. Sci. Manuf. 43 (2012) 363–369, https://doi.org/10.1016/j.compositesa.2011.12.010.
[35] N. Chawla, Y.-L. Shen, Mechanical behavior of particle reinforced metal matrix composites, Adv. Eng. Mater. 3 (2001) 357–370, https://doi.org/10.1002/1527-2648(200106)3:6<357::AID-ADEM357>3.0.CO;2-I.
[36] A. Veillère, A. Sundaramurthy, J.-M. Heintz, J. Douin, M. Lahaye, N. Chandra, et al., Relationship between interphase chemistry and mechanical properties at the scale of micron in Cu–Cr/CF composite, Acta Mater. 59 (2011) 1445–1455, https://doi.org/10.1016/j.actamat.2010.11.006.
[37] X.F. Su, H.R. Chen, D. Kennedy, F.W. Williams, Effects of interphase strength on the damage modes and mechanical behaviour of metal–matrix composites, Compos. Appl. Sci. Manuf. 30 (1999) 257–266, https://doi.org/10.1016/S1359-835X(98)00158-4.
[38] W. Jincheng, Y. Gencang, The energy dissipation of particle-reinforced metal-matrix composite with ductile interphase, Mater. Sci. Eng., A 303 (2001) 77–81, https://doi.org/10.1016/S0921-5093(00)01880-3.
[39] R.M. German (Ed.), Front-matter. Sintering: from Empirical Observations to Scientific Principles, Butterworth-Heinemann, Boston, 2014, p. i, https://doi.org/10.1016/B978-0-12-401682-8.00017-3.
[40] S. Sanzaro, C. Bongiorno, P. Badalà, A. Bassi, G. Franco, P. Vasquez, et al., Inter-diffusion, melting and reaction interplay in Ni/4H-SiC under excimer laser annealing, Appl. Surf. Sci. 539 (2021) 148218, https://doi.org/10.1016/j.apsusc.2020.148218.
[41] J. Trapp, B. Kieback, Fundamental principles of spark plasma sintering of metals: part I – Joule heating controlled by the evolution of powder resistivity and local current densities, Powder Metall. 62 (2019) 297–306, https://doi.org/10.1080/00325899.2019.1653532.
[42] Y. Holovenko, L. Kollo, M. Saarna, R. Rahmani, T. Soloviova, M. Antonov, et al., Effect of lattice surface treatment on performance of hardmetal - titanium interpenetrating phase composites, Int. J. Refract. Metals Hard Mater. 86 (2020) 105087, https://doi.org/10.1016/j.ijrmhm.2019.105087.
[43] M. Calandri, D. Manfredi, F. Calignano, E.P. Ambrosio, S. Biamino, R. Lupoi, et al., Solution treatment study of inconel 718 produced by SLM additive technique in view of the oxidation resistance, Adv. Eng. Mater. 20 (2018) 1800351, https://doi.org/10.1002/adem.201800351.
[44] S. Wu, S. Zhang, Y. Chu, Z. Hu, J. Luo, Stacked Lamellar matrix enabling regulated deposition and superior thermo-kinetics for advanced aqueous Zn-ion system under practical conditions, Adv. Funct. Mater. 31 (2021) 2107397, https://doi.org/10.1002/adfm.202107397.
[45] M. Chmielewski, K. Pietrzak, M. Teodorczyk, S. Nosewicz, D. Jarząbek, R. Zybała, et al., Effect of metallic coating on the properties of copper-silicon carbide composites, Appl. Surf. Sci. 421 (2017) 159–169, https://doi.org/10.1016/j.apsusc.2016.12.130.
[46] V. Dhand, S. Bharadwaj, K. Amareshwari, V. Himabindu, K.Y. Rhee, S.-J. Park, et al., Facile, soot free approach toward synthesis of carbon nanoropes via chemical vapor deposition of acetylene in the presence of MnFe2O4 coated on stainless steel, Appl. Surf. Sci. 359 (2015) 797–804, https://doi.org/10.1016/j.apsusc.2015.10.208.
[47] Y. Wang, D. Zhang, J. Cai, Fabrication and characterization of flaky core–shell particles by magnetron sputtering silver onto diatomite, Appl. Surf. Sci. 363 (2016) 122–127, https://doi.org/10.1016/j.apsusc.2015.11.148.
[48] Y.-S. Park, C.Y. An, P.K. Kannan, N. Seo, K. Zhuo, T.K. Yoo, et al., Fabrication of dendritic silver-coated copper powders by galvanic displacement reaction and their thermal stability against oxidation, Appl. Surf. Sci. 389 (2016) 865–873, https://doi.org/10.1016/j.apsusc.2016.08.008.
[49] J. Ru, Y. Hua, C. Xu, J. Li, Y. Li, D. Wang, et al., Morphology-controlled preparation of lead powders by electrodeposition from different PbO-containing choline chloride-urea deep eutectic solvent, Appl. Surf. Sci. 335 (2015) 153–159, https://doi.org/10.1016/j.apsusc.2015.02.045.
[50] S. Nosewicz, B. Romelczyk-Baishya, D. Lumelskyj, M. Chmielewski, P. Bazarnik, D. Jarząbek, et al., Experimental and numerical studies of micro- and macromechanical properties of modified copper–silicon carbide composites, Int. J. Solid Struct. 160 (2019) 187–200, https://doi.org/10.1016/j.ijsolstr.2018.10.025.
[51] D.M. Jarząbek, C. Dziekoński, W. Dera, J. Chrzanowska, T. Wojciechowski, Influence of Cu coating of SiC particles on mechanical properties of Ni/SiC co-electrodeposited composites, Ceram. Int. 44 (2018) 21750–21758, https://doi.org/10.1016/j.ceramint.2018.08.271.
[52] M. Smith, ABAQUS/Standard User's Manual, 2009, Version 6.9.
[53] M.K. Hassanzadeh-Aghdam, M.J. Mahmoodi, R. Ansari, A comprehensive predicting model for thermomechanical properties of particulate metal matrix nanocomposites, J. Alloys Compd. 739 (2018) 164–177, https://doi.org/10.1016/j.jallcom.2017.12.232.
[54] M.K. Hassanzadeh-Aghdam, R. Ansari, M.J. Mahmoodi, Thermal expanding behavior of carbon nanotube-reinforced metal matrix nanocomposites-A micromechanical modeling, J. Alloys Compd. 744 (2018) 637–650, https://doi.org/10.1016/j.jallcom.2018.02.100.
[55] A. Moradi, R. Ansari, M.K. Hassanzadeh-Aghdam, S.-H. Jang, Thermomechanical behavior of carbon nanotube/graphene nanoplatelet-reinforced shape memory polymer nanocomposites: a micromechanics-based finite element approach, Eur. J. Mech. Solid. 107 (2024) 105360, https://doi.org/10.1016/j.euromechsol.2024.105360.
[56] J. Besson, Continuum models of ductile fracture: a review, Int. J. Damage Mech. 19 (2010) 3–52, https://doi.org/10.1177/1056789509103482.
[57] G. Rousselier, Ductile fracture models and their potential in local approach of fracture, Nucl. Eng. Des. 105 (1987) 97–111, https://doi.org/10.1016/0029-5493(87)90234-2.
[58] Brocks Steglich, Micromechanical modelling of damage and fracture of ductile materials, Fatig. Fract. Eng. Mater. Struct. 21 (1998) 1175–1188, https://doi.org/10.1046/j.1460-2695.1998.00078.x.

[59] A.L. Gurson, Continuum Theory of Ductile Rupture by Void Nucleation and Growth. Part I. Yield Criteria and Flow Rules for Porous Ductile Media, U.S. Energy Research and Development Administration, 1975.
[60] V. Tvergaard, A. Needleman, Analysis of the cup-cone fracture in a round tensile bar, Acta Metall. 32 (1984) 157–169, https://doi.org/10.1016/0001-6160(84)90213-X.
[61] G. Vadillo, J. Fernández-Sáez, An analysis of Gurson model with parameters dependent on triaxiality based on unitary cells, Eur. J. Mech. Solid. 28 (2009) 417–427, https://doi.org/10.1016/j.euromechsol.2008.10.005.
[62] Z.L. Zhang, C. Thaulow, J. Ødegård, A complete Gurson model approach for ductile fracture, Eng. Fract. Mech. 67 (2000) 155–168, https://doi.org/10.1016/S0013-7944(00)00055-2.
[63] M. Feucht, D. Sun, T. Erhart, T. Frank, Recent Development and Applications of the Gurson Model, 2006.
[64] V. Tvergaard, Resistance curves for mixed mode interface crack growth between dissimilar elastic–plastic solids, J. Mech. Phys. Solid. 49 (2001) 2689–2703, https://doi.org/10.1016/S0022-5096(01)00074-6.
[65] V. Tvergaard, J.W. Hutchinson, The influence of plasticity on mixed mode interface toughness, J. Mech. Phys. Solid. 41 (1993) 1119–1135, https://doi.org/10.1016/0022-5096(93)90057-M.
[66] Z.-H. Jin, G.H. Paulino, R.H. Dodds, Cohesive fracture modeling of elastic–plastic crack growth in functionally graded materials, Eng. Fract. Mech. 70 (2003) 1885–1912, https://doi.org/10.1016/S0013-7944(03)00130-9.
[67] V. Tvergaard, On localization in ductile materials containing spherical voids, Int. J. Fract. 18 (1982) 237–252, https://doi.org/10.1007/BF00015686.
[68] J. Zhang, Q. Ouyang, Q. Guo, Z. Li, G. Fan, Y. Su, et al., 3D Microstructure-based finite element modeling of deformation and fracture of SiCp/Al composites, Compos. Sci. Technol. 123 (2016) 1–9, https://doi.org/10.1016/j.compscitech.2015.11.014.
[69] Y.S. Suh, S.P. Joshi, K.T. Ramesh, An enhanced continuum model for size-dependent strengthening and failure of particle-reinforced composites, Acta Mater. 57 (2009) 5848–5861, https://doi.org/10.1016/j.actamat.2009.08.010.
[70] Nuruzzaman Md, Ariful Islam M, Ashraful Alam M, Hadi Shah MA, Tanveer Karim AMM. (PDF) Structural, elastic and electronic properties of 2H- and 4H-SiC. ResearchGate n.d. https://www.researchgate.net/publication/281707085_Structural_elastic_and_electronic_properties_of_2H-_and_4H-SiC (accessed January 14, 2025).
[71] O. Pabst, M. Schiffer, E. Obermeier, T. Tekin, K.D. Lang, H.-D. Ngo, Measurement of Young's modulus and residual stress of thin SiC layers for MEMS high temperature applications, Microsyst. Technol. 18 (2012) 945–953, https://doi.org/10.1007/s00542-011-1419-3.
[72] M. Xu, D. Shin, P.M. Sberna, R. van der Kolk, A. Cupertino, M.A. Bessa, et al., High-strength amorphous silicon carbide for nanomechanics, Adv. Mater. 36 (2024) 2306513, https://doi.org/10.1002/adma.202306513.
[73] H.W. Swift, Plastic instability under plane stress, J. Mech. Phys. Solid. 1 (1952) 1–18, https://doi.org/10.1016/0022-5096(52)90002-1.
[74] J.V. Fernandes, D.M. Rodrigues, L.F. Menezes, M.F. Vieira, A modified swift law for prestrained materials, Int. J. Plast. 14 (1998) 537–550, https://doi.org/10.1016/S0749-6419(98)00027-8.
[75] T. Lei, J.L. Wardini, O.K. Donaldson, T.J. Rupert, In situ mechanical testing of an Al matrix composite to investigate compressive plasticity and failure on multiple length scales, J. Mater. Sci. 56 (2021) 8259–8275, https://doi.org/10.1007/s10853-021-05789-2.
[76] M. Maździarz, S. Nosewicz, Atomistic investigation of deformation and fracture of individual structural components of metal matrix composites, Eng. Fract. Mech. 298 (2024) 109953, https://doi.org/10.1016/j.engfracmech.2024.109953.
[77] X. Lu, M. Ridha, B.Y. Chen, V.B.C. Tan, T.E. Tay, On cohesive element parameters and delamination modelling, Eng. Fract. Mech. 206 (2019) 278–296, https://doi.org/10.1016/j.engfracmech.2018.12.009.
[78] W. Węglewski, P. Pitchai, K. Bochenek, G. Bolzon, R. Konetschnik, B. Sartory, et al., Experimental and numerical investigation of the deformation and fracture mode of microcantilever beams made of Cr(Re)/Al2O3 metal–matrix composite, Metall. Mater. Trans. A 51 (2020) 2377–2390, https://doi.org/10.1007/s11661-020-05687-3.